Distribution Agreement

Signature:

______________________________ ______________

Erin E. Schuler Date

Investigating Fundamental Mechanisms of Peptide Insertion into Membranes

By

Erin E. Schuler

Doctor of Philosophy

Chemistry

____

R. Brian Dyer

Advisor

____

Vince Conticello

Committee Member

____

Khalid Salaita

Committee Member

Accepted:

____

Lisa A. Tedesco, Ph.D.Dean of the James T. Laney School of Graduate Studies

____

Date

Investigating Fundamental Mechanisms of Peptide Insertion into Membranes

By

Erin E. Schuler

B.S. Youngstown State University, 2008

Advisor: R. Brian Dyer, PhD

An abstract of

A dissertation submitted to the Faculty of the

James T. Laney School of Graduate Studies of Emory University

in partial fulfillment of the requirements for the degree of

Doctor of Philosophy

in Chemistry

2015

Abstract

Thirty percent of the human genome is committed to production of membrane proteins. The importance of membrane proteins transcends all living organisms as these macromolecules serve as the gatekeepers to many processes that maintain homeostasis and cellular communication. Essential to adopting proper structure and function is the ability for membrane proteins to insert into target membranes. Despite the significance of this process, many questions concerning the fundamental mechanism of how insertion is achieved remain. For example, how do dynamic protein structures facilitate insertion? What are the energetics that govern this process? What role does the membrane play? Perhaps an even greater deficit in the field is the ability to couple membrane dynamics to those of proteins. Both membranes and proteins represent complex classes of macromolecules. In addition, the dynamics that govern these structures challenge the temporal resolution of many available techniques often used to study these systems. Thus, the nature of protein-membrane interactions necessitates development of time-resolved methods capable of capturing such dynamic processes.

This dissertation aims to examine the mechanisms that drive spontaneous insertion of peptides into membranes, coupling membrane dynamics to those of the inserting peptides. In brief, the first half of this dissertation focuses on characterizing the dynamics of the fluid phase transition of model membranes and then utilizes the physical properties of membrane phases to examine spontaneous insertion of a small antimicrobial peptide, Mastoparan X (MPX). To accomplish this, the gel to fluid phase transformation was characterized in model d62-DPPC unilamellar vesicles by temperature-jump infrared spectroscopy. These studies revealed that d62-DPPC vesicles achieve the fluid phase state in only hundreds of nanoseconds by propagation of disorder from the edges of the membrane facets. Utilizing the ability to rapidly trigger the fluid phase state of the d62-DPPC membranes, the insertion rate of MPX was determined. These results indicate that insertion occurs within a few hundred microseconds, and importantly, determine the thermodynamic parameters that govern MPX insertion into a model membrane thereby establishing an exciting new methodology to probe spontaneous insertion of proteins into membranes.

The second half of this dissertation examines peptide insertion as it relates to the mechanism of influenza A hemagglutinin (HA) protein, and its role in viral membrane fusion. It is hypothesized that early steps in HA-mediated membrane fusion are driven by folding of the coiled-coil motif Loop-40 (L40) in response to acidification of the endosome upon viral uptake. Ultimately, this process promotes extension of the HA fusion peptide to the surface of the host endosome, priming insertion of HA. In this dissertation, the folding mechanism of HA L40 peptide was studied by temperature-jump infrared and fluorescence spectroscopy. These results reveal a complex folding pathway, where three possible intermediates are accessed between the folded and unfolded state. Additionally, formation of the coiled-coil core is rapidly achieved, taking only ~10^{-4} s to fold. Lastly, an infrared fusion assay was successfully developed using combinations of isotope labeled and non-isotope labeled lipids to establish a platform for simultaneous monitoring of HA driven insertion and membrane fusion. Together, these studies add to the fundamental understanding of dynamic protein-membrane interactions, focused specifically on the underlying mechanisms that govern spontaneous insertion of peptides into membranes.

Investigating Fundamental Mechanisms of Peptide Insertion into Membranes

By

Erin E. Schuler

B.S. Youngstown State University, 2008

Advisor: R. Brian Dyer, PhD

A dissertation submitted to the Faculty of the

James T. Laney School of Graduate Studies of Emory University

in partial fulfillment of the requirements for the degree of

Doctor of Philosophy

in Chemistry

2015

Acknowledgments

It has been said that it takes a village to raise a child and I think the same applies for a PhD. First and foremost, I would like to thank my advisor, Brian Dyer, for giving me the opportunity to learn from him and for teaching our group that discipline, hard work and persistence, regardless of short-term disappointments, is always the formula for long-term success. I am grateful for his willingness to share his knowledge with his students and for believing in all of us, especially in moments when we doubt ourselves. I would also like to thank my committee members Khalid Salaita and Vince Conticello for their constant support and guidance throughout this process.

I am fortunate to have taken up the bench next to a diverse group of talented lab mates. For current and former members of the Dyer group, you have made the Dyer lab a fun and fulfilling environment to work in. I would especially like to thank the folding group and Brandon Greene, Samuel Ban-seok Jeong, Bryant Chica and Gokul Raghunath for their friendship both in and out of the lab. To the students that I have had the pleasure of mentoring, especially Gokul, Casey Anthony, Linda Liu, and Paula Tyler, watching them develop as scientists has been one of the most rewarding experiences of my graduate career. I would also like to thank another important lab member, Laura Dyer, for her love and support and for taking the time to always prepare much anticipated, delicious, home-cooked meals for all of our group celebrations. In addition, a special thanks to Ann Dasher and Steve Krebs for the many things they do that often go unnoticed, but mostly I would like to thank them for their friendship.

To my friends that I have met during my time at Emory: Ashley Bagwell, Yoshi Narui, Pravin Muthu, Samantha Iamurri, Daniel Stabley, Carol Jerchenko, and Jennifer

Bon thank you for many years of learning and laughter, my life is certainly enriched because all of you are in it. I appreciate all of my early mentors including: Peter Norris, Nina Stourman and David Gemmel for their early mentorship and encouragement as much of their influence guided me to pursuing a PhD in chemistry.

I am forever grateful to my parents for their unconditional love and support throughout my PhD and always, for the many sacrifices they have made to raise and educate their children. To my siblings, Billy, Brian, Christopher and Trish, thank you for giving me such big shoes to fill. I would especially like to thank my brother Christopher for having encouraged and supported my passion for science as long as I can remember. I am fortunate to have a wonderful extended family. With that said, I would also like to thank my Aunt Anne and Uncle John for all of their help and encouragement, and for making Atlanta feel like a home away from home. Most importantly, I would like to thank Kevin Yehl for his unwavering love and support. For being the most genuine, kind and accepting person I have ever known which constantly has pushed me to try to be the very best version of myself. Without him this would not have been possible.

List of Frequently Used Abbreviations

Abbreviation	**Full Name**
LUV	Large Unilamellar Vesicle
SUV	Small Unilamellar Vesicle
FTIR	Fourier Transform Infrared Spectoscopy
CD	Circular Dichroism
MPX	Mastoparan X
D62-DPPC	1,2-dipalmitoyl(d62)-*sn*-glycero-3-phosphocholine
TEM	Transmission Electron Microscopy
AUC	Analytical Ultracentrifugation
Trp	Tryptophan
T-Jump	Temperature-Jump
CHCA	α-Cyano-4-hydroxycinnamic acid
L40	Loop-40
FP	Fusion Peptide
HA	Hemagglutinin

Table of Contents

List of Figures

List of Tables

Chapter 1: A General Introduction to Dynamic Protein-Membrane Interactions

1.1 Introduction

1.1.1 Historical Perspective

The year 1855 marked the first description of a barrier that surrounds the most basic unit of life. We would later come to call this barrier—the plasma membrane. In 1895, Charles Ernest Overton related permeation of small molecules to their partition coefficient between oil and water indicating that membranes are hydrophobic substances composed mostly of lipids and cholesterol.[1] By 1917, Langmuir concluded that lipids in monolayers were oriented, where the polar headgroups of the lipid molecules were arranged in a way that allowed them to face water, while the greasy hydrocarbons chains oriented themselves towards the air interface. [2] In 1925, Gorter and Grendel discovered that the surface area of lipids extracted from red blood cells was twice that of the surface area determined from microscopy images.[3] Together, these observations ultimately lead to the idea that cellular membranes were composed of a bilayer of lipids, where the hydrophobic acyl chains faced inwards making a hydrophobic membrane core and the polar head groups oriented to the exterior, contacting the water interface.[1,3]

The notion of proteins as a critical part of membrane structure was not put forth until a decade after Gorter and Grendal's bilayer model of cellular membranes.[1] Set into motion by Jim Danielli and Hugh Davson (1935), their studies had a particular emphasis on the proteins that were adsorbed onto the membrane surface. Ultimately these studies led to the trilayer model of membranes where proteins were thought to create a continuous network along the membrane surface.[4] In 1958, transmission electron microscopy broke the resolution limit of optical spectroscopy, thus allowing for J. David Robertson to capture an image of the plasma membrane. The year 1958 also marked a major advancement in x-ray crystallography, where for the first time, crystal structures provided atomic pictures of protein structure.[5]

1.2 Membrane Theory

1.2.1 The Fluid Mosaic Model

In 1966, Lenard and Singer connected the role of hydrophobic residues to the high propensity of membrane proteins to contain alpha helical domains.[1] Made possible by advancing technology in X-ray crystallography, this relationship ultimately leads Singer and Nicholson to develop the fluid mosaic model in 1972.[6] One of the most prolific models to date, this model integrates the role of proteins and lipids in membrane structure, where two main types of proteins exist: peripheral membrane proteins associated with the membrane surface, and integral membrane proteins that span the bilayer. This model is significant not only for being the first functional model of the plasma membrane but also that it provides an inkling of dynamic membrane protein interactions suggesting protein lateral motion within the plasma membrane.

1.2.2 The Mattress Model

Mouritsen and Bloom modified the fluid mosaic model, developing the plasma membrane as a complex surface. The fluid mosaic model implies that proteins associated with the membrane are homogeneously distributed within a uniform fluid state. The mattress model (1984) expands on the fluid mosaic model to include the concept of hydrophobic matching where a mismatch in length of either the hydrophobic membrane core or integrated proteins would expose hydrophobic segments to water. [7]As a thermodynamic incentive to minimize these unfavorable interactions, lipids and proteins alike would segregate to select for neighboring molecules that most closely match the desired hydrophobic length. Ultimately this effect would lead to clusters of proteins non-homogeneously distributed within the cellular membrane, a deviation from the uniformity proposed in the fluid mosaic model.

1.2.3 Modern Perspective on Membrane Theory

The fluid mosaic model continues to be the basis for all modern adaptations of membrane theory, however, we now understand membranes to be a composite of a diverse array of lipids in a crowded environment abundant in proteins.[8,9] As a result, current models describing membrane theory portray biological membranes as incredibly complex asymmetric surfaces. As suggested in these modern adaptations of the fluid mosaic model, the effects of membrane content and macromolecular crowding on lipid order present intriguing implications for the role of membrane fluidity on membrane protein dynamics. Even simple prokaryotic organisms like B. *subtilis* dedicate entire signaling pathways to modulating fluid phase state,[10] as tension derived from heightened lipid order has a direct effect on the function of the organisms membrane proteins. The case of B. *subtilis* offers a remarkable example of dynamic protein-lipid interactions on the membrane surface driving communication between the outside and inside of a cell. Although the fluid mosaic model does imply that dynamic protein-protein and protein-lipid interactions are significant to the structure and function of biological membranes, it does not provide a quantitative framework for understanding the fundamental mechanisms driving these interactions, and there are few experimental studies that provide quantitative measure of the dynamics.

1.3 Dynamic interactions between membranes and proteins enhanced by lipid order

1.3.1 Hydrophobic Matching

Both the fluid mosaic model and the mattress model create a platform for the notion of dynamic protein-membrane interactions. In the case of the fluid mosaic model, proteins can readily achieve lateral diffusion across the membrane given the uniformly fluid state of the membrane. The mattress model implies more sophisticated dynamics between proteins and membranes in the suggestion that proteins and lipid alike have the capacity to organize within the membrane, such that the membrane is divided into clusters of molecules with similar properties. These concepts were bolstered with the birth of raft theory,[11] the idea that the lipid constituents surrounding proteins in the membrane are likely very different than the ensemble. Furthermore, the presence of small molecules like cholesterol can enhance membrane rigidity, thereby increasing membrane order. [12] Raft theory went one step further to suggest that the lipids surrounding membrane proteins have a direct effect on protein function. These early ideas of dynamic “cell sorting” have also contributed to our understanding of how cellular organelles, e.g. Golgi apparatus, organize proteins in preparation of vesicular transport. [12]

1.3.2 Membrane Protein Folding

In addition to protein organization and function, most membrane proteins require interaction with the membrane to properly fold. One of the earliest contributions to the field of membrane protein folding occurred in 1980 when the fluid mosaic model was less than a decade old. Khorana et al. discerned the relationship between the primary sequence of globular membrane proteins and structural predictably.[13]Shortly thereafter, the light-harvesting, proton-pump and seven helix bundle bacterhodopsin from archaebacteria H. *salinarium* was successfully isolated, unfolded and refolded in vitro.[14] Early models for membrane protein folding were limited to simple two –state models, where the first stage of folding was associated with folding of individual helices, followed by intramembrane helix oligomerization.[14] The folding of membrane proteins was soon directly related to membrane order using the same protein model in early folding studies involving bacterhodopsin. These experiments ultimately related lipid composition, i.e. lipid length and rigidity, to membrane curvature and the perceived force that lipids induce on a folding protein. Increasing membrane rigidity by modulating lipid composition resulted in significantly slower rate constants for formation of the apoprotein intermediate, which is the rate-limiting step of bacterhodopsin folding. This was the first example illustrating how lipids directly affect membrane protein folding.[15]

1.3.3 Insertion of Proteins into Membranes

Tightly coupled to the concept of membrane protein folding is protein insertion into membranes. In general, the proteins that participate in insertion can be categorized as either assisted inserters or spontaneous inserters.[16,17,18] Assisted inserters are thought to insert co-translationally, and are assisted by complex chaperones and translocons, e.g. Sec Y pathway in gram-negative bacteria.[19] Examples of spontaneous inserters include antimicrobial peptides, viral fusion peptides and amyloidgenic peptides. Despite the prevalence and importance of insertion in many biological arenas, the mechanism of protein insertion into membranes is poorly understood. Many experimental methods suited to study this interaction either lack the time resolution to capture the dynamics of protein insertion or lack the versatility to couple membrane dynamics to those of the protein.

1.4 Biomedical Relevance of Protein insertion into Membranes: Viral Pathogenicity, Antimicrobial Peptides and Therapeutics

Beyond the fundamental understanding of dynamic membrane protein interactions, understanding the mechanistic nuances of insertion of proteins into membranes is applicable to our understanding of pathogenicity in viral systems. A hallmark example of this is hemagglutinin (HA) protein found on the influenza virus. In the lifecycle of influenza, viral membrane fusion is mediated by insertion and refolding of the HA protein.[20] This general mechanism for membrane fusion is conserved in most viral systems and is vital to the infectivity of viruses. In addition to the role of insertion in viral systems, insertion is also critical to the mechanism of many antimicrobial peptides (AMPs), as this class of proteins is primarily effective by targeting and disrupting a number of pathogenic membranes. The effectiveness of AMPs has made them a promising target for the pharmaceutical industry. However, understanding the mechanism of insertion and membrane disruption will greatly enhance rational design of molecules that can be used to target and insert into membranes associated with pathogenic organisms.

1.5 Aim and Scope of Dissertation

The most comprehensive models of membranes were conceived in the 1970s and 1980s. What is abundantly clear from the evolution of membrane theory is that the early models still greatly persist today. To truly characterize the dynamic nature of membranes and membrane proteins both experimental and theoretical methods must be able to resolve the molecular detail of membrane components, a methodology still lacking. This dissertation highlights the use of infrared spectroscopy in combination with other biophysical methods to address this limitation and aims to couple the dynamics of membranes and proteins, specifically examining the role of the fluid phase state of membranes on the mechanistic underpinnings of peptide insertion into membranes.

In summary, Chapter 2 will characterize dynamics of the gel to fluid phase transition in model DPPC bilayer vesicles using temperature-jump infrared spectroscopy. These spectroscopic results, in conjunction with theoretical modeling, define a plausible mechanism describing the fluid phase transition of membranes. Chapter 3 capitalizes on the control of membrane phase modulation learned from Chapter 2's findings to study the mechanism of dynamics of protein insertion using the helical antimicrobial peptide mastoparan X (MPX) as a model system. In addition to probing peptide insertion, infrared spectroscopy also allows for direct comparison of lipid dynamics to those of the protein upon protein insertion. Chapters 4 and 5 detail the immediate biological relevance for studying protein insertion by examining mechanisms promoting membrane fusion in influenza hemagglutinin (HA) protein. More specifically, Chapter 4 examines the folding of the trimeric L40 peptide, a portion of HA critical to the pH dependent triggering of HA extension. This step is essential to the mechanism of HA as it results in presentation of the fusion peptide to host endosomes for insertion. Chapter 5 outlines preliminary studies focused on developing an infrared assay for studying the insertion of the fusion peptide and subsequent membrane fusion without the use of fluorophores or other perturbing labels. Together these studies lay the foundation for studying dynamic membrane protein interactions with high molecular and temporal resolution, thus addressing some of the most pertinent limitations to the field.

1.6 References

1. Heimburg, T. Thermal Biophysics of Membranes. Wiley-VCH Publishers, 2007.

2. Langmuir, I. The constistution and fundamental properties of solids and liquids. II. Liquids. J. Am. Chem. Soc. 1917, 39 (9),1848–1906.

3. Gorter, E. and Grendel, F. On Biomolecular layers of lioids on the chromocytes of the blood. JEM. 1925, 41(4) 439-443.

4. Robertson, J. D. A molecular theory of cell membrane structure. Quatrième Congrès International de Microscopie Électronique.1960,159-171.

5. Kendrew J. C. et al. A Three-Dimensional Model of the Myoglobin Molecule Obtained by X-Ray Analysis. Nature. 1958, 181 (4610), 662–6.

6. Singer, S.J., Nicolson, G.L.The fluid mosaic model of the structure of cell membranes. Science. 1972,175(4023), 720-31.

7. Mouritsen, O. G., and Bloom, M. Mattress model of lipid-protein interactions in membranes. Biophys J. 1984, 46(2),141–153.

8. Nicolson, G. L. The Fluid—Mosaic Model of Membrane Structure: Still relevant to understanding the structure, function and dynamics of biological membranes after more than 40 years. Biochimica et Biophysica Acta : biomembranes. 2014, 1838 (6), 1451-1466.

9. Engelman, D. M. Introduction Membranes are more mosaic than fluid. Nature 438, 578-580.

10. Cybulski, L.E., Albanesi,D., Mansilla, M. C., Altabe, S., Aguilar, P.S. and Mendoza, D. Mechanism of membrane fluidity optimization: isothermal control of the *Bacillus subtilis* acyl-lipid desaturase . Molec. Microbiol. (2002) 45(5), 1379–1388.

11. Israelachvili, J. N. Theoretical considerations on the asymmetric distribution of charged phospholipid molecules on the inner and outer layers of curved bilayer

membranes. Biochim. Biophys. Acta. 1973, 323, 659-663.

12. Jensen, M. O. and Mouritsen, O. G.Lipids do influence protein function—the hydrophobic matching hypothesis revisited. Biochimica et Biophysica Acta: Biomembranes. 2004, 1666 (1-2), 205–226.

12. Krause, M.R., Regen, S.L. The structural role of cholesterol in cell membranes: from condensed bilayers to lipid rafts. Acc Chem Res. 2014, 47(12),3512-21.

13. Khorana, H. G. et al. The bacteriorhodopsin gene. Proc. Natl. Acad. Sci. 1981, 78(11), 6744-6748.

14. Popt, J-L., Gerchman, S-L., Engelman, D-M. Refolding of bacteriorhodopsin in lipid bilayers: A thermodynamically controlled two-stage process. Journal of Molecular Biology. 1987, 198(4), 655–676.

15. Booth, P.J., Riley, M.L., Flitsch, S.L., Templer, R.H., Farooq, A., Curran, A.R., Chadborn, N., Wright, P. Evidence that bilayer bending rigidity affects membrane protein folding. Biochemistry. 1997, 36(1), 197-203.

16. Neupert, W. and Herrmann, J.M. Translocation of Proteins into Mitochondria. Annul. Rev. of Biochem. 2007, 76, 723-749.

17. Rapoport, T. A. Protein translocation across the eukaryotic endoplasmic reticulum and bacterial plasma membranes. Nature. 2007, 450, 663-669.

18. Wickner, W.T. Lodish, H. F. Multiple mechanisms of protein insertion into and across membranes. Science. 1985, 230(4724), 400-407.

19. Mori, H. and Ito, K. The Sec protein-translocation pathway.Trends Microbiol. 2001, 9(10), 494-500.

20. Carr, C. M., Chaudry, C. and Kim, P.S. Influenza hemagglutinin is spring-loaded by a

metastable native conformation. 1997, 94 (26)14306–14313.

21. Zasloff, M. Antimicrobial peptides of multicellular organisms. Nature. 2002, 415, 389-395.

22. Wade, et al. Proline-rich antimicrobial peptides: potential therapeutics against antibiotic-resistant bacteria. Amino Acids. 2014, 46(10), 2287-2294.

Chapter 2: Dynamics of the Gel to Fluid Phase Transformation in Unilamellar DPPC Vesicles

Reprinted with permission from Nagarajan, S., Schuler, E. E., Ma, K., Kindt, J. T., and Dyer, R. B. Dynamics of the Gel to Fluid Phase Transformation in Unilamellar DPPC Vesicles. The Journal of Physical Chemistry B. 2012, 116 (46), 13749-13756. Copyright 2012 American Chemical Society.

2.1 Introduction

Lipid dynamics play a critical role in a wide range of cell membrane phenomena. An important example is the dynamic formation of nanoscale liquid ordered assemblies in the cell membrane, which have been postulated to organize components to achieve specific functionality, including simple mechanical functions, signal transduction, ion transport, and membrane trafficking.[1–6] These processes may involve changes in lipid structure and dynamics and associated changes in local membrane fluidity and permeability. Understanding the dynamic organization of membranes requires elucidating the underlying structures and dynamics that span many orders of magnitude in length and time scales, from the molecular to the macroscopic. Model membrane systems have played an important role in the study of the molecular structures and dynamics that underlie macroscopic phenomena. Although the cell membrane is a mixture of hundreds of lipid types, the phase behavior of simple model phospholipid bilayers is of interest not only as a starting point for understanding the cell membrane, but also for potential applications in bionanotechnology. Here we focus on the dynamics of a phase transition in a simple model unilamellar vesicle that may serve as a basis for elucidating the dynamics of more complex phenomena in the lipid bilayer.

The phospholipid 1,2-dipalmitoyl-*sn*-glycero-3-phosphocholine (DPPC) forms stable, well-characterized unilamellar lipid vesicles. The equilibrium phase behavior of DPPC bilayers has been extensively studied. The equilibrium phase behavior of unilamellar DPPC bilayers exhibits four distinct phases, the crystal (Lc′), gel ($L\beta'$), ripple ($P\beta'$), and fluid or liquid-crystalline ($L\alpha$) phases in order of increasing temperature. The sharpest and most endothermic transition (ΔH = 33 kJ/mol) is the “main transition” between the highly ordered gel phase and the disordered fluid phase. Notably, the main transition ($T\text{m}$ = 41 °C, conveniently near normal human body temperature) produces a sharp increase in permeability that is the basis for the use of DPPC liposomes to deliver anticancer drugs selectively to solid tumors subjected to hyperthermia therapy.[7,8] The underlying molecular changes in this main transition include the conversion of lipid acyl chains from the nearly all-trans configuration to one having an increased number of gauche "kinks," and associated increases in the interfacial area per lipid and in the lipid conformational disorder and mobility.[4] The $L\beta'$ to $P\beta'$ transition has been observed in large unilamellar vesicles (LUV),[9] although it is not clear how the 10–15 nm periodicity of the ripple phase is influenced by the 50 nm radius of curvature.[10] All of these phase changes influence the membrane structure and dynamics. In the past several decades, the focus of studies of membrane phase behavior has been on understanding the thermodynamics and structures of the gel and fluid ordered and disordered phases and the transitions between them. The dynamics of the gel to fluid phase transition is less well understood, however, due to the lack of structural specificity of the time-resolved methods used to observe the nanosecond to millisecond events.[11–15] Relaxation methods have been the primary tool used to explore the dynamics of phase transitions, probed by light scattering,[16,17] calorimetry,[18,19] ultrasound,[20] and dielectric relaxation.[20] A hierarchy of relaxation times is observed due to the complexity of the physical changes involved in phase transitions. These methods do not directly determine the molecular origin of the observed relaxation times, so the results are generally interpreted using physical models and in light of more structurally specific measurements of the dynamics. The fastest relaxation modes have been assigned to the correlation times of lipid head groups (10^{-11}–

10^{-10} s), to chain segmental motions (10^{-9} s), to lateral diffusion of lipid monomers (10^{-8} s), and to gauche–trans isomerization (10^{-6} s) by analogy to NMR measurements of specifically deuterium labeled lipids.[21] Slower relaxation processes (10^{-6}–10^{-2} s) have been assigned to domain fluctuations, based on statistical mechanical models that predict a critical slowing of the lifetime near the transition temperature.[19,20] More recently, efforts have focused on developing molecular models of the dynamics of lipid phase transitions using molecular dynamics simulations.[22–25] Experimental evidence is still needed to complement these efforts and to test the validity of the computational models. Insight about how well the force fields predict the observed lipid dynamics is useful for evaluating simulations of more complex phenomena such as the formation of cholesterol containing liquid ordered phases.

In this work, we have used an integrated experimental and theoretical approach to investigate the lipid dynamics during the gel to fluid phase transition and subsequent relaxation of the vesicle structure in 100 nm homogeneous perdeuterated d62-DPPC unilamellar vesicles. We have applied a new experimental approach to this problem consisting of laser temperature jump (*T*-jump) initiation coupled with time-resolved infrared spectroscopy to follow the molecular details of the phase transition from nanoseconds to milliseconds. *T*-jump methods allow the exploration of the dynamics far from equilibrium, particularly for a *T*-jump that is large compared to the width of the phase transition. Previous studies have used laser *T*-jump coupled with X-ray methods to study the structural transitions of lipid bilayers in water, but did not resolve the dynamics.[26,27] IR spectroscopy is a powerful, nonperturbing technique that is sensitive to acyl chain conformation, headgroup environment, and water interactions. Time-resolved

IR spectroscopy can follow these structures on time scales ranging from the ultrafast conformational dynamics of the monomer to the slower global relaxation of a lipid bilayer and associated processes such as water permeation.[28] Therefore, it is possible to connect the molecular dynamics with the macroscopic phenomena using this approach. Deuterated DPPC was chosen, since the CD2 symmetric stretch falls in a clear region of the FTIR spectrum and hence is useful to probe membrane properties in the presence of other components, including peptides and other (nondeuterated) lipids. The infrared transients that characterize the gel to fluid phase transition of DPPC are complex, extending from the nanosecond to the millisecond time scales. The dominant phase is fast (submicrosecond) and is well modeled as a partial melting of the gel domains, initiated at pre-existing defects at the edges of the faceted structure of the gel phase. Molecular dynamics simulations of a buckled lipid bilayer support the model of rapid melting proceeding from the partially disordered edge structure.

2.2 Materials and Methods

2.2.1 Preparation of d62-DPPC LUVs

The d62-DPPC lipids and extrusion kit were purchase from Avanti Polar Lipids, Inc. A 25-mg portion of d62-DPPC in chloroform was pipetted into a 2 mL glass vial and dried by N_2 gas, after which the sample was placed under vacuum for at least 5 h to ensure complete removal of solvent. The dried lipid film was hydrated with 300 μL of 20 mM sodium phosphate buffer at pH 7.4 with 150 mM NaCl for at least 30 min followed by at least five freeze thaw cycles starting at a temperature above the Tm and then quenching to 4 °C on ice. Unilamellar vesicles of 100 nm were prepared by extruding the hydrated solution 15 times or more through a polycarbonate filter having pore openings of 100 nm diameter, at a temperature 10 – 20 °C above the *T*m of the vesicles. Transmission electron micrographs of the vesicles indicate that they are within the expected size range. For the equilibrium and temperature jump experiments, the samples were used immediately after the extrusion procedure.

2.2.2 Equilibrium FTIR

Equilibrium FTIR temperature-dependent spectra were recorded on a Varian 3100 FTIR spectrometer equipped with liquid nitrogen cooled mercury cadmium telluride (MCT) detector. The spectra were the result of 256 scans recorded at a resolution of 2 cm^{-1}. The d62-DPPC lipid vesicles were prepared as described above in buffer containing 20 mM sodium phosphate and 150 mM sodium chloride at a pH* of 7.4, in D_2O [pH* refers to the uncorrected (for D_2O) pH-meter reading at 25 °C]. The d62-DPPC lipid concentration for IR experiments is approximately 30 mM. A split IR cell composed of CaF_2 windows was utilized with a path length of 100 μm to record the spectrum of both the reference (D_2O buffer solution) and the sample (d62-DPPC lipid vesicles in D_2O buffer) side of the IR transmission cell under identical conditions at each temperature. The temperature of the IR cell was controlled by a water bath, and the sample temperature was measured by a thermocouple attached to the cell. The absorbance spectra of the lipid vesicles were determined from the negative logarithm of the ratio of the single beam spectra of the sample to the reference side of the IR split cell at each temperature.

2.2.3 Temperature-Jump Infrared Spectroscopy

The *T*-jump time-resolved IR apparatus used to measure the lipid relaxation kinetics in this study has been previously described.[29,30] The *T*-jump experiment is a pump–probe experiment in which a short pulsed (10 ns) 1.91 μm laser pulse constitutes the pump that is absorbed by the D_2O solvent and causes a rapid (10 ns) *T*-jump in the sample. The *T*-jump initiates the gel to fluid phase transformation. A quantum cascade laser (Daylight Solutions Inc., Poway, CA) tunable either in the 1565–1735 cm^{-1} or the 2035–2145 cm^{-1} region is used to probe structural changes in the sample as the system relaxes to a new equilibrium at the final temperature in response to the *T*-jump. The changes in transmission of the IR probe beam are detected by a fast (200 MHz) photovoltaic MCT detector (Kolmar Technologies, Newburyport, MA). The 1.91 μm (10 ns fwhm Gaussian pulse width, ~30 mJ/pulse) pump radiation is obtained from a H_2 (g) filled Raman shifter (1 Stokes shift) pumped by a 10 Hz repetition rate Q-switched DCR-4 Nd:YAG laser (Spectra Physics, Mountain View, CA) and is absorbed by weak combination bands in the D_2O solution. This pump wavelength was chosen to achieve nearly uniform heating in the pump–probe overlap region, because 87% of the pump intensity is transmitted through the 100 μm path length sample cell. The same split cell used for the equilibrium FTIR experiments was used for the kinetic measurements with the reference D_2O buffer compartment serving as an internal thermometer to determine the magnitude of the *T*-jump. The lipid relaxation transients were extracted by subtracting the change in absorbance of the reference (D_2O buffer) from the sample (d62-DPPC in D_2O buffer) in response to the *T*-jump. The kinetic traces were recorded from 10^{-9} to 10^{-2} s using a Tektronix 7912 digitizer capable of switching the time base at 5 different time points during the acquisition, to achieve uniform sampling over 7 decades in time. The data analysis was performed in IGOR Pro (Wavemetrics, Inc.).

2.2.4 Simulation Methods

A DPPC gel was created as previously described.[25] Thirty-two lipids arranged in the crystalline conformation were solvated by 800 waters, and first equilibrated at 273 K for 10 ns at 1 bar pressure. The structure was then replicated 8-fold along the X axis and 2-fold along the Y axis to yield a 512-lipid, 12 800-solvent box with dimensions 26.7 × 5.0 × 7.2 nm, with the tail tilt aligned with the Y axis. This structure was then subject to uniaxial compression over a 3.0 ns simulation at 310 K, with a reference pressure of 400 bar in the X direction and 1 bar in the Y and Z. The resulting structure (dimensions 21.8 × 5.1 × 8.8 nm) contained two sharp bends, but maintained nearly regular packing of its tails. This buckled structure was subject to 50 ns further MD simulation under fixed X and Y box dimensions, with pressure coupling in the Z dimension set at 1 bar pressure, at temperatures above and below the estimated transition temperature of 308 K previously determined for this force-field.[25] Simulations were performed using Gromacs 4.5[31] using the united-atom DPPC forcefield of Berger et al.[32] and a time step of 2 fs. Electrostatic forces were treated using the particle-mesh Ewald method[33] with standard Gromacs parameters. Temperature and pressure coupling were achieved using the Berendsen method.[34]

2.3 Results and Discussion

2.3.1 Equilibrium FTIR

FTIR spectroscopy is ideally suited to characterize the equilibrium phase behavior of DPPC vesicles. Figure 2.1A shows the temperature-dependent (10 to 44 °C) FTIR spectra of LUV in D_2O buffer, in the region of the CD_2 symmetric stretching vibration of d62-DPPC. The IR absorption band for non-deuterated DPPC CH_2 symmetric stretching vibration is centered at 2850 cm^{-1}, but this mode is shifted to 2089 cm^{-1} for the deuterated lipid. The CD_2 symmetric stretch of the d62-DPPC vesicles is shifted from 2089 cm^{-1} at 10 °C to 2093 cm^{-1} at 44 °C and the bandwidth increases by ~5–6 cm^{-1}. Both changes are consistent with the melting of the ordered gel phase to a disordered

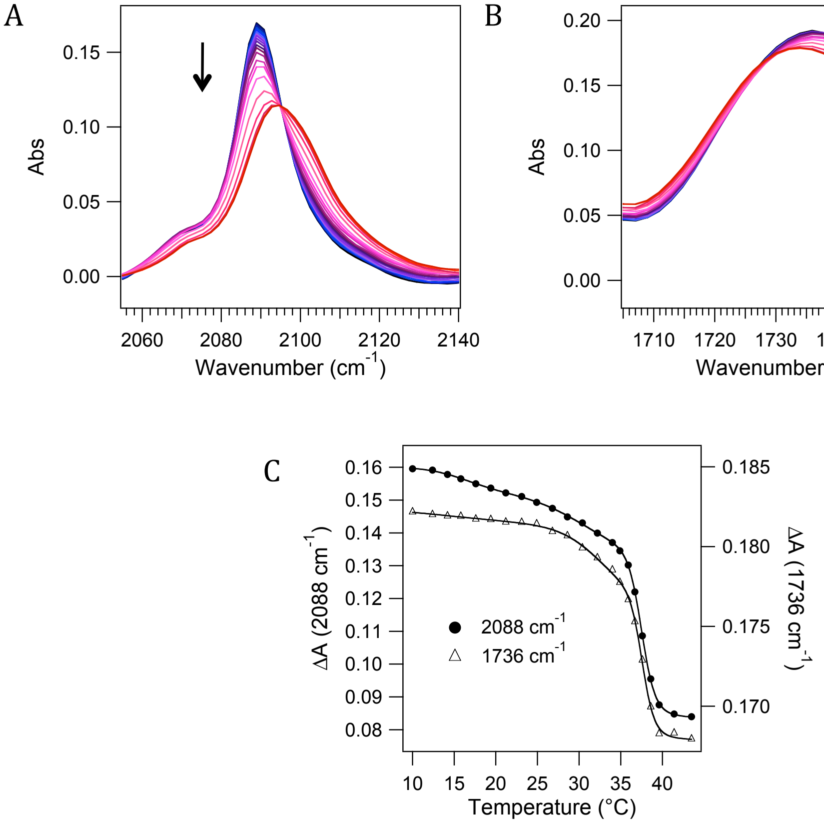

Figure 2.1. Temperature dependent FTIR spectra of d62-DPPC LUV in the range of 10 - 44 °C in ~2 °C increments in (A) the CD_2 symmetric stretch and (B) the ester C=O stretch spectral regions. Arrows indicate direction of absorbance change with increasing temperature (blue = cold, red = hot). (C) Thermal phase transition of d62-DPPC obtained by plotting the intensity of the CD_2 stretch (2088 cm^{-1}) and C=O stretch (1736 cm^{-1}) versus temperature. The two curves are scaled separately for ease of comparison (note that the 1736 cm^{-1} ΔA values are significantly smaller than those at 2088 cm^{-1}). Solid lines are fits to a three sigmoid equation (eq 1).

fluid or liquid crystalline phase. The shift to higher frequency is due to a loss of the mode coupling (inter- and intrachain) that is present in the tightly packed, nearly all-trans conformation (this coupling lowers the CD_2 stretching frequency), but is absent in the disordered phase due to isomerization of the acyl chain to include some gauche conformations. These gauche “kinks” disrupt intrachain mode coupling due to unfavorable geometry, and the concomitant increase in interchain distance disrupts interchain coupling. The increase in bandwidth is due to the increased acyl chain disorder, causing an increase in the inhomogeneous broadening. The weaker band at 2070 cm^{-1} is attributed to the symmetric stretching vibration of the terminal methyl group of the lipid acyl chains. All of these changes are completely reversible upon cooling of the solution back to the starting temperature, on the time scale of the FTIR measurement (minutes).

Figure 2.1B presents the temperature-dependent FTIR spectra of lipid headgroup ester carbonyl stretching (C=O) vibration. This mode occurs at 1738 cm^{-1} for the gel phase at 10 °C and is shifted to 1736 cm^{-1} in the liquid crystal phase at 44 °C. The C=O vibration band is sensitive to the local dielectric of the interface and to hydrogen bonding to water. Therefore, it is a sensitive indicator of the hydration of the membrane in the lipid headgroup region. At 44 °C, the C=O vibration is downshifted, suggesting that the headgroup is better hydrated in the fluid than in the gel phase. Figure 2.1C shows the melt curves derived from the temperature dependence of the intensities of the CD_2 vibration at 2088 cm^{-1} and the C=O vibration at 1736 cm^{-1}. The solid lines are fits to a three-sigmoid function to describe the three transitions between the four distinct phases:

the crystal (Lc') to gel ($L\beta'$) transition ($T\mathrm{m}_1$), the gel ($L\beta'$) to ripple ($P\beta'$) transition ($T\mathrm{m}_2$), and the ripple ($P\beta'$) to fluid or liquid-crystalline ($L\alpha$) transition ($T\mathrm{m}_3$):

$$\Delta A = \frac{A_1}{1+e^{(T_{m1}-T)/r_1}} + \frac{A_2}{1+e^{(T_{m2}-T)/r_2}} + \frac{A_3}{1+e^{(T_{m3}-T)/r_3}} + b \qquad (1)$$

The melt temperatures of each of these transitions determined from the fit of the CD_2 stretch data are $T\mathrm{m}_1 = 16.4 \pm 0.8$ °C; $T\mathrm{m}_2 = 30.7 \pm 0.8$ °C; and $T\mathrm{m}_3 = 37.5 \pm 0.1$ °C, respectively. The C=O data yield the same transition temperatures within experimental error. The gel to ripple, and ripple to fluid phase transition temperatures derived from the fits are in agreement with other spectroscopic and calorimetric results ($T\mathrm{m}$ = 35–37.5 °C).[35–37] The small variations in the main phase transition temperature reported for d62-DPPC by different groups may be attributed to the different accuracies of the measurements or to variability in the vesicle size (radius of curvature) and hence specific melt temperature.

2.3.2 Temperature-jump Infrared Spectroscopy

Temperature-jump initiation coupled with time-resolved infrared spectroscopy is a highly sensitive technique that allows us to directly follow the dynamics of any system that undergoes a temperature dependent structural transition within a time range of nanoseconds to hundreds of milliseconds.[38] We have used a 10 ns laser induced *T*-jump to initiate the main phase transformation in d62-DPPC LUV, and probed the resulting dynamics using the CD_2 symmetric stretching vibration at 2089 cm^{-1}. Figure 2.2A shows the time-resolved IR absorbance of d62-DPPC LUV monitored at 2089 cm^{-1} in response to a laser induced *T*-jump from various starting temperatures. The *T*-jump magnitude is 4–7 °C and the initial temperature is below *T*m in all cases. A range of starting temperatures was probed to determine the temperature dependence of the relaxation rates.

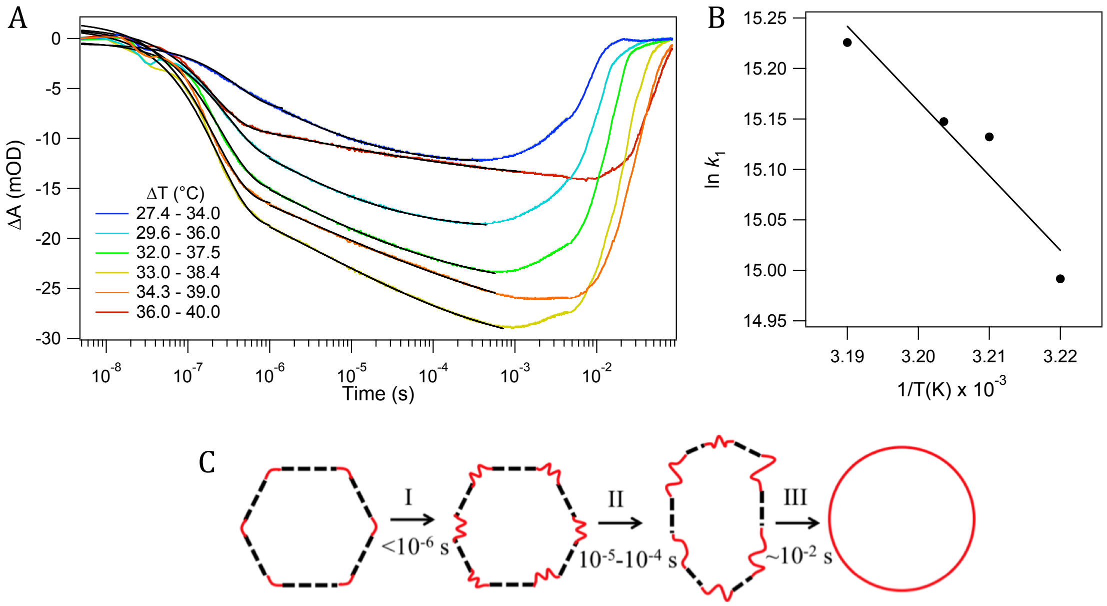

Figure 2.2. LUV dynamics following a laser induced *T*-jump. (A) Relaxation kinetics of d62-DPPC LUV monitored at 2089 cm^{-1} (CD_2 symmetric stretch) in response to a *T*-jump of magnitude of 4–7 °C. The legend indicates the initial and final temperatures for each jump. The kinetic traces are the average of 2500 laser shots. The solid lines are fits to eq 2. (B) Arrhenius plot of the initial rate for jumps to the fluid phase. (C) Cartoon of stages in vesicle melting. Dashed lines represent gel phase domains, red curves represent fluid phase regions.

A transient bleach is observed at this probe frequency, as expected for the transition from an ordered gel to disordered liquid crystalline phase, based on the equilibrium FTIR data presented in Figure 2.1. The *T*-jump IR transients observed at 1712 cm^{-1}, which monitors the ester C=O stretch of the lipid headgroup, show the same general features as those observed for the CD_2 vibrations. Both are dominated by an initial response on the nanosecond time scale, followed by an extended nonexponential phase on the microsecond time scale. The 1712 cm^{-1} transients are noisier, however, due to the smaller absorbance change for this band, hindering accurate fitting of these data.

The relaxation transients exhibit complex kinetics spanning several orders of magnitude in time. The transients could not be fit to a single exponential or to a multiexponential function and hence were fit to single exponential (the dominant phase), crossing over smoothly to a stretched exponential (eq 2):

$$\begin{aligned} \Delta abs(t) &= c_1\left[\exp(-t/\tau_1)-1\right], \quad 0<t<t_c \\ &= c_2\exp(-t/\tau_2)^{\alpha}-c_{tot}, \quad t>t_c \end{aligned} \tag{2}$$

This function resembles the "coupling model" function used to describe relaxation in glass-forming systems[39] in its inclusion of a crossover time tc between single-exponential and stretched-exponential regimes, but differs in specifics. The time constants of the initial single-exponential component and the stretched exponential are represented by $\tau 1$ and $\tau 2$, the stretch factor by α, the onset time of the stretched exponential regime by tc, and the total amplitude of the transient change in absorbance by $c$tot. From these five independently variable fitting parameters, the amplitude prefactors of the single and stretched exponential stages (c1 and c2) are obtained from the constraints of continuity in the function and its first derivative at tc (see Appendix A2.3 for details). Optimal fit values are given in Table 2.1. The transient corresponding to the lowest temperature *T*-jump, from 27.4 to 34 °C, is equally well fit by a simple stretched exponential function. This *T*-jump is completely within the gel ($L\beta'$) to ripple ($P\beta'$) phase transition. All of the other *T*-jumps reported here extend into the fluid phase. The distinct single exponential regime is apparently characteristic of the main transition.

The transients for *T*-jumps within the main transition are best fit by eq 2. Significant portions of the transient absorbance change are completed both before and after the crossover time, which lies near 1 μs. A number of interpretations are possible for the initial rapid response and subsequent slowing-down of the change in acyl chain CD_2 IR absorbance. The initial single-exponential component of the response could be attributed to changes in tail packing within the phases, while the slow component corresponds to melting of gel phase into fluid. This interpretation is not consistent with the observed equilibrium temperature dependent FTIR data, however, which show absorbance changes of at most –1.3 mOD per degree below the main transition onset. The predicted change is not great enough to account for the observed magnitude of the initial fast response.

A more likely origin of the fast initial kinetic transient is the physical conversion of gel phase to fluid phase DPPC. Assuming the fast initial changes in IR absorbance reflect conversion of gel or ripple phase DPPC to fluid phase DPPC, we can estimate the initial rate of melting (–*dA*gel/*dt*) from the initial rate in change of the signal (*d*Abs2089/*dt*, Table 1) and the total change in equilibrium absorbance over the phase transition (ΔAbs2089,total) determined from the melt curve. The total gel vesicle area, *A*total is assumed to equal 2.5 × 104 nm^2 based on the 100 nm average diameter of the LUV. The initial rate values (–*dA*gel/*dt*) calculated for each *T*-jump are summarized in Table 2.1.

Schrader et al. have recently identified a relaxation process with a time constant "τ0" of ~100 ns in the ultrasonic spectra of DMPC vesicles near their *T*m, (within 2°) tentatively assigned to "local shape deformations of the vesicles".[20] We propose that the fast melting phase observed in the IR *T*-jump experiments is a nonequilibrium manifestation of this mode, and provides insight into its nature. The shift in the CD_2 IR absorption feature at this time scale indicates that this mode arises from the transition of lipid tails between ordered and disordered environments, and that (when driven by a large enough perturbation) the mode amplitude can encompass the phase change of a substantial fraction of the lipids in the vesicle. Under equilibrium conditions, the mode could be associated with smaller-amplitude excursions of the ordered/disordered domain boundaries, coupled to local shape deformations. In ultrasonic spectra, the mode is not observed at temperatures lower than *T*m – 2 K, which could either indicate that the structure associated with this mode is absent at low *T* or that the mode amplitude is very weak. In the current experiments, the submicrosecond response appears unambiguously

T-Jump (°C)	**Tau$_1$ (ns)**	**Tau$_2$ (ns)**	**α**	**t$_c$ (ns)**	**c$_1$ (mOD)**	**c$_2$ (mOD)**	**c$_{tot}$ (mOD)**	**-dAbs$_{2089}$/dt (mOD/ns)**	**-dA$_{gel}$/dt (nm^2/ns)**	**-dA$_{gel}$/dt (predicted)**
27-34	256	318	0.234	450	6	22	12	0.024	60	43
29-36	310	426	0.236	910	12	23	19	0.040	67	41
32-37	308	5142	0.297	1129	16	15	23	0.052	42	35
33-38	268	1127	0.312	1061	21	16	29	0.073	43	35
34-39	264	1027	0.259	1043	17	16	26	0.066	36	30
36-40	244	603	0.129	1002	10	14	14	0.040	24	26

Table 2.1. T-Jump IR (2089 cm^{-1}) Relaxation Parameters from Fits to Eq. 2

and without a lag period in *T*-jump profiles starting from temperatures as low as 7° below *T*m, suggesting that the structure from which the mode develops is already present.

2.3.3 Simulations

The conventional kinetic mechanism for a melting transition involves first the slow, activated nucleation of domains of the fluid phase, followed by a more rapid size increase of new domains, and finally a slow annealing phase as defects between domains are resolved through large-scale realignments. The fast response can be reconciled with this model if the barrier to nucleation of the new phase is negligible, which would require the presence of defects that can act as nucleation sites. Since faceting has been observed for vesicles of diameter 50–200 nm using cryo-electron microscopy,[40,41] defects at the ridges joining facets are likely an intrinsic feature of the gel-phase LUV structure. We hypothesize that curvature stress and packing defects at these ridges produce an effective local transition temperature lower than the bulk *T*m, or in other words that the lipids at these defects are in a fluid state at equilibrium even below *T*m. These premelted ridges are candidates for nucleation sites for fast melting of the individual facets. Evidence to support premelting at ridges, which has been proposed previously to explain temperature-dependent permeability trends in LUVs,[7] comes from atomistic molecular dynamics simulations of ridge-like structures. Uniaxial compression of a gel-phase bilayer sheet was used to prepare a buckled gel-phase structure with localized regions of high curvature. The effect of temperature on this structure is shown in Figure 2.3.

At 308 K (the estimated *T*m for DPPC using this force field[25]), the orderly packing of the gel phase, evident from the nearly straight and evenly spaced tails, is disrupted in the zones of high curvature. At 303 K, disordering at the bends is also apparent in more narrow zones, while at 298 K one bend is disordered while the other retains regular packing on the outer leaflet. At 313 K, melting has extended from the bend into one leaflet of the flat portion of the bilayer, and at 318 K one of the two flat sections of bilayer is entirely melted. The simulation results therefore confirm that lipids at ridge sites may be disordered in an otherwise ordered bilayer below *T*m. Furthermore, the results suggest that the extent of premelting depends on *T* and that above *T*m melting proceeds rapidly from the ordered/disordered boundary. Ordered/disordered boundaries have also been described as equilibrium features of molecular models of the ripple

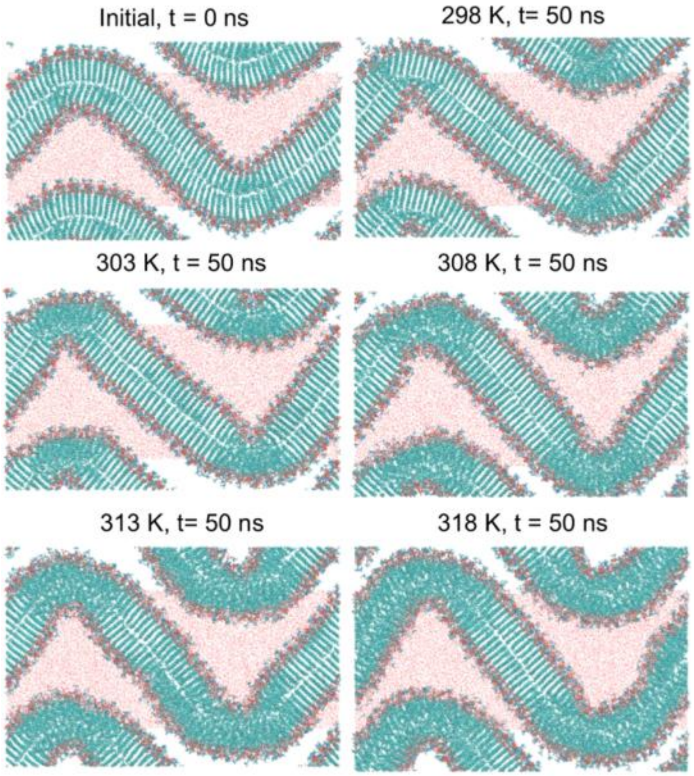

Figure 2.3. Snapshots from molecular dynamics simulations of buckled gel-phase DPPC bilayer. Partial replicas of the lipid component are shown to indicate continuity of the bilayer across periodic boundaries; solvent is shown (red dots) in primary box only.

phase[42] and may play a role similar to that of ridge defects as nucleation sites for melting.

As an additional test of the hypothesis that the submicro-second change in IR spectrum reflects rapid initial melting from defects, we compare the observed rates to predictions based on estimates for the lengths of the boundary edges and the rate of transition from gel to fluid. For instance, a regular icosahedron of area equal to that of a 100 nm diameter vesicle would have a total ridge length of 1.6 μm; assuming that melting proceeds in both directions from each ridge gives a total interfacial front length of 3.2 μm. The postnucleation rate of the melting transition in DPPC has been estimated experimentally in terms of the velocity of advancement of a gel/fluid interface of 2×10^{-3} m K^{-1} s–^{1} × ($T - T$m).[10] In the vesicles at equilibrium at the starting temperature of the *T*-jump, the boundary between the premelted ridge region and the ordered region will be localized wherever the effective *T*m determined by local curvature equals the actual temperature. Substituting the lower temperature as the effective local *T*m, the initial rate of melting after the *T*-jump is therefore 2×10^{-3} m K^{-1} s^{-1} × ΔT. Multiplying the estimate of 3.2 μm for the total front length by this rate produces initial rates of the same order as those seen in experiment (final column of Table 2.1). Therefore, we conclude that the initial fast response can be plausibly attributed to melting nucleated at ridge defects. Additional evidence that supports this interpretation comes from an Arrhenius analysis of the fast exponential phase, shown in Figure 2.2B. The activation energy derived from this analysis is 62 kJ/mol, about double the reported enthalpy of melting for DPPC vesicles (29–30 kJ/mol),[9] and in good agreement with a previous estimate from simulations of the apparent activation energy for retraction of the gel phase edges of 68 kJ/mol.[25]

After one microsecond, the initial exponential melting phase smoothly converts to a highly stretched exponential melting phase that spans several orders of magnitude in time. To explain the tremendous slowing-down of the melting process, we consider the approximately 24% area expansion involved in the gel-fluid transition. As area expands, the resulting surface pressure (negative surface tension) will raise the effective melting temperature and slow the melting process.[43] This surface pressure may result in wrinkling of the newly formed fluid phase, shown in step I of Figure 2.2C. Without any mechanism for its relaxation, accumulation of surface pressure is expected to produce a simple exponential decrease in the gel fraction, with melting asymptotically slowing down as the effective melting temperature approaches the actual temperature (see Appendix A2.4). However, the vesicle in its partially melted state will tend to distort to dissipate this surface pressure and associated curvature stresses, a process that likely involves a hierarchy of undulatory modes with different relaxation times, including collective shape changes to the entire vesicle (Figure 2.2C, step II). In glass-forming systems, crossover from single- to stretched-exponential relaxation dynamics is attributed to a transition from localized to collective relaxation modes; in the present system, the onset of the stretched exponential dynamics seen in the IR transients can be attributed to a transition from independent melting of individual domains to melting that is limited by the rate of surface stress relaxation through cooperative reorganization.

The final stage in relaxation requires solvent transport through the membrane to enable the vesicle to expand its internal volume to reach a minimized curvature stress at its new, higher surface area (Figure 2.2C, step III). The typical time scale for volume relaxation following changes in osmotic pressure in fluid-phase LUVs is of the order 10^{-}

^{2}–10^{-1} s.[44] Our experiments provide indirect evidence that water transport through the membrane driven by the expanding vesicle occurs on the hundreds of microseconds to milliseconds time scale. The water diffusion process may not be complete within the observation time of the *T*-jump, however, because the transient absorbance never reaches the expected equilibrium value from the FTIR measurements. The maximum ΔA reached (before the solution begins to cool), expressed as a percentage of the equilibrium value is 100, 79, 71, 62, and 36% for jumps to 36, 37.5, 38.4, 39, and 40 °C, respectively. Clearly, a significant fraction of the amplitude is not captured for jumps to a final temperature that is above *T*m. The further the jump into the fluid phase, the longer the relaxation time due to both the slow collective relaxation and water diffusion processes and therefore less of the expected change occurs within the fixed time window of the *T*-jump.

At still longer times, the small volume of solution (roughly 10 nL) heated by the laser begins to cool back to the initial temperature with a lifetime of 12 ms, causing the vesicles to return to the gel phase. The cooling time is nearly constant over the temperature range probed, based on the behavior of the buffer reference solution. In contrast, the apparent cooling time of the vesicle solutions becomes progressively longer as the *T*-jump reaches higher temperatures, as shown in Figure 2.2A. Therefore, we conclude that the recovery kinetics of the gel phase are slow compared to the cooling time, and they become slower as the final temperature is increased. For jumps to a final temperature below *T*m, which are less than halfway through the transition, the 100 ms repetition time of the experiment is sufficient for complete recovery of the initial gel phase (the transient signals in Figure 2.2A recover back to the baseline). At temperatures above 40 °C, however, the recovery becomes slow enough that the transient signal becomes progressively smaller and eventually disappears entirely due to the buildup of a steady-state population of the fluid state. Slowing the laser repetition rate from 10 to 1 Hz allows the sample to recover sufficiently between laser pulses so that the transient signal reappears. We are unable to quantitatively determine the kinetics of reforming the gel phase because they are convoluted with the thermal transport kinetics occurring on nearly the same time scale. It is clear, however, that the kinetics depend strongly on the extent of melting of the vesicles. Nucleation of the gel phase from the completely melted vesicles occurs on the hundreds of milliseconds time scale, such that reforming the gel phase is only observed by drastically slowing down the repetition rate of the experiment.

2.4 Conclusions

We have determined the dynamics of the main gel to fluid phase transition in DPPC large unilamellar vesicles. Although the dynamics of the phase transformation is complex, the dominant phase is extremely fast, with a relaxation time of a few hundred ns. A practical consequence of the fast transformation is the possibility of rapidly triggering membrane processes that depend on membrane fluidity, using a laser-induced *T*-jump. Therefore, it should be possible to study the dynamics of important membrane processes ranging from protein insertion, folding, aggregation, and function using this approach. Since the fundamental dynamics of the phase transition are so fast, related phenomena that involve similar molecular mechanisms, such as the transition from a liquid-ordered to a liquid-disordered state, likely occur on a similar time scale or even faster. For example, tighter lipid packing is a characteristic of liquid-ordered domains and therefore the liquid ordered to disordered transition involves changes in lipid conformation and interfacial surface area, albeit of a smaller magnitude. Rapid transitions in local order and fluidity may play a functional role in many processes that take place within the membrane or at its interface.[6,45,46] For example, cells may control protein insertion, folding, and function by controlling membrane fluidity. A cell can modulate the membrane fluidity by changing the local membrane composition and therefore modulate trafficking or assembly of membrane bound complexes. The ability to rapidly switch membrane fluidity may act as a gating mechanism for such processes. The dynamics of lipids within the bilayer is also an important issue that influences many membrane processes. Our results provide a direct measure of important lipid dynamics during a phase transition and subsequent overall relaxation of the vesicle. The results provide the fundamental basis for understanding and predicting the dynamics of such processes.

2.5 References

1. Brown DA, London E. Annu. Rev. Cell Dev. Biol. 1998;14:111–136.

2. Simons K, Ikonen E. Nature. 1997;387:569–572.

3. Herreros J, Ng T, Schiavo G. Mol. Biol. Cell. 2001;12:2947–2960

4. Nagle JF, Tristram-Nagle S. Biochim. Biophys. Acta. 2000;1469:159–195.

5. London E. Biochim. Biophys. Acta. 2005;1746:203–220.

6. Lingwood D, Simons K. Science. 2010;327:46–50.

7. Mills JK, Needham D. Biochim. Biophys. Acta. 2005;1716:77–96.

8. Needham D, Dewhirst MW. Adv. Drug Delivery Rev. 2001;53:285–305.

9. Mason PC, Gaulin BD, Epand RM, Wignall GD, Lin JS. Phys. Rev. E. 1999;59:921–928.

10. Kranenburg M, Smit B. J. Phys. Chem. B. 2005;109:6553–6563.

11. Kharakoz DP, Shlyapnikova EA. J. Phys. Chem. B. 2000;104:10368–10378.

12. Genz A, Holzwarth JF. Eur. Biophys. J. 1986;13:323–330.

13. Laggner P, Kriechbaum M. Chem. Phys. Lipids. 1991;57:121–145.

14. Genz A, Holzwarth JF, Tsong TY. Biophys. J. 1986;50:1043–1051.

15. Caffrey M. Annu. Rev. Biophys. Biophys. Chem. 1989;18:159–186.

16. Tsong TY, Kanehisa MI. Biochemistry. 1977;16:2674–2680.

17. Blume A, Hillmann M. Eur. Biophys. J. Biophys. Lett. 1986;13:343–353.

18. Vanosdol WW, Johnson ML, Ye Q, Biltonen RL. Biophys. J. 1991;59:775–785.

19. Grabitz P, Ivanova VP, Heimburg T. Biophys. J. 2002;82:299–309.

20. Schrader W, Halstenberg S, Behrends R, Kaatze U. J. Phys. Chem. B. 2003;107:14457–14463.

21. Smith RL, Oldfield E. Science. 1984;225:280–288.

22. Marrink SJ, Risselada J, Mark AE. Chem. Phys. Lipids. 2005;135:223–244.

23. Risselada HJ, Marrink SJ. Soft Matter. 2009;5:4531–4541.

24. Leekumjorn S, Sum AK. Biochim. Biophys. Acta. 2007;1768:354–365.

25. Coppock PS, Kindt JT. J. Phys. Chem. B. 2010;114:11468–11473.

26. Tenchov B, Koynova R, Rapp G. Biophys. J. 1998;75:853–866.

27. Rappolt M, Pabst G, Rapp G, Kriechbaum M, Amenitsch H, Krenn C, Bernstorff S, Laggner P. Eur. Biophys. J. Biophys. Lett. 2000;29:125–133.

28. Lewis RNAH, McElhaney RN. Methods Mol. Biol. 2007;400:207–226.

29. Dyer RB, Gai F, Woodruff WH, Gilmanshin R, Callender RH. Acc. Chem. Res. 1998;31:709–716.

30. Williams S, Causgrove TP, Gilmanshin R, Fang KS, Callender RH, Woodruff WH, Dyer RB. Biochemistry. 1996;35:691–697.

31. Hess B, Kutzner C, van der Spoel D, Lindahl E. J. Chem. Theor. Comp. 2008;4:435–447.

32. Berger O, Edholm O, Jähnig F. Biophys. J. 1997;72:2002–2013.

33. Essman U, Perera L, Berkowitz ML, Darden T, Lee H, Pedersen LG. J. Chem. Phys. 1995;103:8577–8592.

34. Berendsen HJC, Postma JPM, DiNola A, Haak JR. J. Chem. Phys. 1984;81:3684–3690.

35. Fraile MV, Patrón-Gallardo B, López-Rodríguez G, Carmona P. Chem. Phys. Lipids. 1999;97:119–128.

36. Lewis RNAH, Pohle W, McElhaney RN. Biophys. J. 1996;70:2736–2746.

37. Singh H, Emberley J, Morrow MR. Eur. Biophys. J. 2008;37:783–792.

38. Callender R, Dyer RB. Curr. Opin. Struct. Biol. 2002;12:628–633.

39. Ngai KL. J. Phys.: Condens. Matter. 2000;12:6437–6451.

40. Andersson M, Hamarstrom L, Edwards K. J. Phys. Chem. 1995;99:14531–14538.

41. Ickenstein LM, Arfvidsson MC, Needham D, Mayer LD, Edwards K. Biochim. Biophys. Acta: Biomembr. 2003;1614:135–138.

42. de Vries AH, Yefimov S, Mark AE, Marrink SJ. Proc. Natl. Acad. Sci. U.S.A. 2005;102:5392–5396.

43. Uline MJ, Schick M, Szleifer I. Biophys. J. 2012;102:517–522.

44. Mathai JC, Tristram-Nagle S, Nagle JF, Zeidel ML. J. Gen. Physiol. 2008;131:69–76.

45. Groves JT, Kuriyan J. Nat. Struct. Mol. Biol. 2010;17:659–665.

46. Saxena R, Chattopadhyay A. J. Neurochem. 2011;116:726–733.

Appendix 2: Dynamics of the gel to liquid-crystal phase transformation in lipid bilayer vesicles

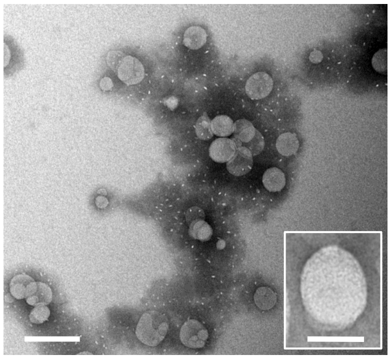

Figure A2.1. Transmission electron micrograph of d62-DPPC lipid vesicles obtained by the extrusion method. Vesicles were negatively stained for 30 seconds with a 1% (w/v) solution of PTA, pH 7.0. Samples were dried under vacuum for 30 minutes prior to imaging. The scale bar for the lower magnification and inset image represent 200 nm and 100 nm respectively.

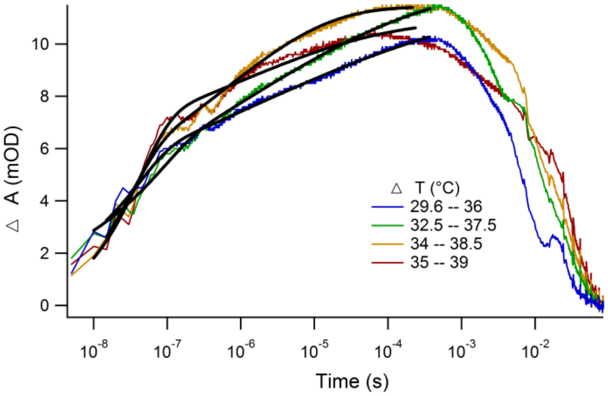

Figure A2.2. Temperature-jump relaxation kinetics of D62-DPPC LUV monitored at 1712 cm^{-1} (C=O vibration) in response to a T-jump of magnitude of 4-7 °C. The kinetic traces are the average of 2500 laser shots. The solid lines are fits to equation 2. Please note: The C=O vibration transient data was collected at 1712 cm^{-1} due to the limitation of the range of probe laser in the experiment, despite the maximum absorbance occurring at 1738 cm^{-1} in the FTIR equilibrium experiments.

A2.3 Relationship Between Fitting Parameters in Equation 2:

Given τ_1, τ_2, α, t_c, and c_{tot}, the constraints on continuity of the function and its first derivative at $t = t_c$ constrain the c_1 and c_2 terms to the following:

$$c_1 = c_{tot}\left[\left(\frac{\tau_2}{\alpha\tau_1}\left(\frac{t_c}{\tau_2}\right)^{1-\alpha} - 1\right)\exp(-t_c/\tau_1) + 1\right]^{-1}$$

$$c_2 = c_1\frac{\tau_2}{\alpha\tau_1}\left(\frac{t_c}{\tau_2}\right)^{1-\alpha}\frac{\exp(-t_c/\tau_1)}{\exp\left[-(t_c/\tau_2)^{\alpha}\right]}$$

A2.4 Derivation of Single Exponential Form for Vesicle Melting

Define A_{gel} as area of system in the gel phase, and assume that in the absence of surface pressure,

$$-\frac{dA_{gel}}{dt} = CL_{bnd}\left(T - T_m\right)$$

where L_{bnd} is the length of the boundary between gel and fluid (treated as constant), C is a constant, and T_m is the transition temperature. The expansion associated with the melting process causes an increase in surface pressure P, which may be relaxed by some process or processes at a rate Γ:

$$\frac{dP}{dt} = -\frac{\chi_{melt}\kappa}{A_{tot}}\frac{dA_{gel}}{dt} - \Gamma\left(P,\ldots\right)$$

where χmelt ≈ 0.24 is the fractional area expansion associated with melting and $\varkappa$ is a surface compressibility modulus. (Because of the possibilities for local buckling, $\varkappa$ is not necessarily the same as the typical compressibility modulus, which relates surface tension to relative increase in area.) The effect of surface pressure (or negative surface tension) is an effective increase in the melting transition temperature by a factor $P\Delta A$melt/ΔHmelt°, which will slow down the melting rate.[43] We can approximate a pressure-dependent melting rate by substituting Tm from equation B1 with a pressure-dependent transition temperature Tm(P):

$$-\frac{dA_{gel}}{dt} = CL_{bnd}\left(T - T_m\left(1 + \frac{P\Delta A_{melt}}{\Delta H^{o}_{melt}}\right)\right)$$

The overall dynamics of melting will then depend on the balance of pressure building up through the area increase associated with melting and the rate of pressure relaxation through changes in vesicle shape and volume, which are implicitly included in the relaxation rate Γ, which would be expected to depend on pressure but may depend on the structural state of the vesicle as well. If we can treat surface relaxation as negligible on the melting time scale, (Γ = 0) then these two equations yield an exponential decay in the gel-phase area until the surface pressure effect on Tm halts further melting:

$$-\frac{A_{gel}(t)}{A_{tot}} = \frac{\Delta H_0}{\chi_{melt}\kappa\Delta A}\left(\frac{T}{T_m(0)} - 1\right)\left(1 - \exp\left(\frac{CL_{bnd}}{A_{tot}}\frac{\chi_{melt}\kappa\Delta A}{\Delta H_0}T_m(0)t\right)\right)$$

Chapter 3: Insertion of Mastoparan X into Model d62-DPPC Lipid Vesicles Triggered by Rapid Thermal Initiation of the Membrane Phase Transition

3.1 Introduction

Protein folding has been an active area of research for decades, but a rising challenge in the field has been acquiring an understanding of how membrane proteins fold. This is a complicated endeavor, as studying membrane protein folding requires not only an understanding of the physical properties of proteins, but intimate knowledge of the membrane surface and the dynamic relationship between proteins and membrane counterparts. It is well known that synthesis of proteins takes place in cellular organelles within the cytoplasm, i.e. ribosomes. Nascent proteins intended to function in the membrane are typically transported unstructured, thus, development of secondary, tertiary, and quaternary structures of membrane proteins is driven by interactions with the target membrane. A common feature of the membrane protein-folding pathway requires protein insertion into target membranes. This interaction is of paramount importance to a number of biological processes including cellular function, cellular signaling, membrane protein folding, membrane fusion, immunological response, viral infectivity and a host of others.[1,2,3,4,5] In addition to the broad application of protein insertion in the biological realm, the population of proteins that participate in insertion is equally as diverse in size, structure and function; entailing everything from large, incredibly hydrophobic proteins assisted by complex chaperons and translocons, to small linear peptides capable of spontaneous insertion into membranes. Although a significant aspect of physiology, mechanistic nuances of protein insertion remain elusive; a deficit likely attributed to a general lack of experimental methods available to study such dynamic processes. The difficulty encountered when pursuing molecular details required to make mechanistic inferences is the inherent complexity of the systems involved. Beyond the basic structural complexity of membranes and protein counterparts, there remains a need for adequate time-resolved methods to capture insertion that have the ability to couple the dynamics of insertion from the perspective of the protein to those of the membrane.

3.1.1 Selection of a Model Peptide

The field of antimicrobial peptides emerged in the late 1980s. Antimicrobial peptides (AMPs) also referred to as host defense peptides (HDPs) are a class of peptides that are typically short sequences, less than 60 amino acids, that yield amphiphilic secondary structures with a net cationic charge.[6,7,8,9,10,11] Typically, AMPs demonstrate a broad-spectrum activity against gram positive bacteria, gram-negative bacteria, a number of viruses and in some instances, may present antifungal properties,[12,13] making many subclasses of AMPs such as defensins, cecropins, magainins, and cathelcidins exciting pharmaceutical targets.[14] The potential utility as therapeutics have given the science around these peptides more momentum in recent history for the ability of AMPs to target multi-drug resistant bacteria with little or no consequence of resistance in return.[15] Although they show much promise, an FDA approved AMP therapeutic has not been realized, given the susceptibility of AMPs to protease degradation, undesirable off-target interactions and high production costs.[14, 15] As a result, the field has turned to rational design of shorter peptides that reduce production costs and minimize toxicity while retaining desirable antimicrobial properties. Despite the current limitations of AMPs as approved therapeutics, this class of peptides do present the possibility of an accessible model to probe coupled dynamics between peptides and membranes, given that a putative mechanism of many AMPs involves direct peptide interaction with target membranes, a property that has been demonstrated in both naturally occurring and synthetic membrane systems. [16]

Mastoparan X (MPX), first described in 1988, is a 14-residue peptide isolated from wasp venom that carries a +4 charge at neutral pH (Figure 3.1).[17] Beyond antimicrobial activity, MPX has been implicated as an agonist of GTP-binding regulatory proteins, mast cell degranulation and subsequent histamine release.[3,17] Although unstructured in an aqueous environment, MPX folds to adopt an α-helical conformation in the presence of both negatively charged and zwitterionic membranes.[16] The putative model for cationic host

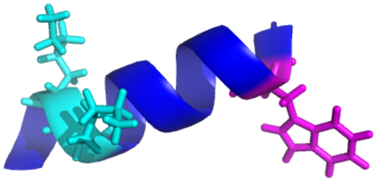

Figure 3.1. Structure and sequence of MPX (PDB: 2CZP), N-INWKGIAAMAKKLL-C.

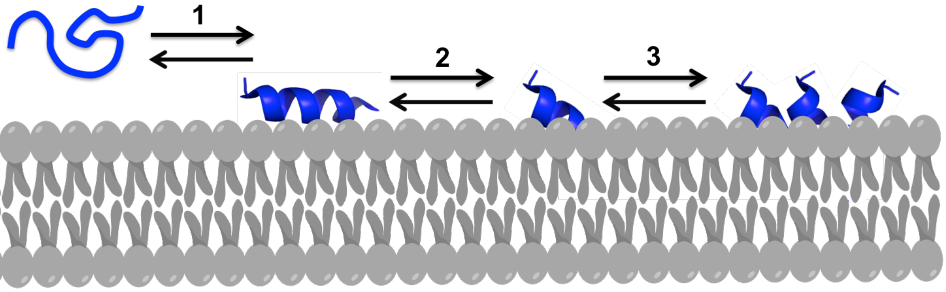

Figure 3.2. Schematic of early possible events of MPX membrane interaction. (1) Association and folding of MPX on membrane surface (2) Insertion of MPX into the membrane (3) Self-association of MPX once inserted

defense peptides suggests insertion occurring normal to an anionic membrane surface while obliquely, or shallowly inserting when interacting with a zwitterionic membrane surface.[18] Previous studies examining the folding and insertion of MPX, and similar peptides, indicate a tightly coupled relationship between the folding of peptides and the ability to traverse membranes. In discerning whether folding of mastoparan X occurs in concert with insertion or if folding occurs prior to insertion, conclusions favor a model where folding of MPX occurs on the highly anisotropic membrane surface upon peptide adsorption, preceding complete insertion of the peptide.[19]

3.1.2 Experimental Approach

Historically, strategies employed to study insertion include mixing experiments, e.g. stopped-flow, however, these methodologies give rise to a classic kinetic conundrum, that is, if the slowest step is the first phase of a multistep process, in this case association of a peptide to a membrane, than faster subsequent steps, i.e. insertion, cannot be purely observed. The previous chapter highlighted rapid initiation of the gel to fluid phase transition of model membranes through temperature-jump experiments. In this instance, we implement a unique strategy to study the insertion of MPX by taking advantage of the rigid features of the saturated DPPC membrane in the gel phase, where the compact structure of the vesicles in the gel-state can exclude the majority of the peptide to the surface of the membrane, allowing us to selectively trigger MPX insertion and accumulation into the membrane through rapid thermal initiation of the gel to fluid phase transition. Our findings in Chapter 2 establish that the bulk of the phase transition is accomplished in less than 1 μs; thus, initiating insertion by control of the membrane fluid phase state provides sufficient time resolution to capture most of the dynamic processes, e.g. insertion, folding and self-association, occurring at the membrane interface. An advantage of this method includes the possibility of allowing the peptide equilibrate with the membrane surface averting limitations consequence of diffusion and/or mixing time.

3.2 Materials and Methods

3.2.1 Peptide Synthesis and Purification

Mastoparan X, INWKGGIAAMAKKLL, was synthesized by standard Fmoc solid phase peptide synthesis utilizing acid-amine coupling on a CEM Liberty 1 peptide synthesizer using a rink-amide resin. Fmoc protected amino acids were purchased from AnaSpec, Inc (Fremont, Inc.). Purification of MpX was completed on a reverse phase C18 column (Phenomenex, Torrance, CA) with HCl as a counterion using a linear gradient of water and acetonitrile. The mass of the purified peptide was confirmed by MALDI-MS using CHCA matrix dissolved in 50:50 mixture of water: acetonitrile. MS confirmed the presence of mastoparan X with a mass equal to 1556 amu.

3.2.2 Lipid Vesicle Preparation.

Deuterated d62-DPPC lipids in chloroform and mini-extruder kit were purchased from Avanti Polar Lipid, Inc. Chloroform was removed by drying the lipid sample with N_2 gas. The resulting film was then placed on the lyophilizer overnight to ensure complete drying of the sample. The lipid film was then rehydrated in 20 mM sodium phosphate buffer, 100 mM NaCl, pH 7.4 above the Tm of the lipid at 55°C for one hour. Following hydration, the sample was subjected to eight consecutive freeze thaw cycles alternating between 0°C and 55°C. The lipid sample was then passed through a mini extruder equipped with a 100 nm polycarbonate filter above the Tm of the lipid at 55°C to yield large unilamellar vesicles. SUVs used in the fluorescence T-jump studies were prepared by the sample hydration method, however instead of extrusion, the samples were subjected to 45 minutes of sonication in a bath sonicator. In both instances, the size distribution of vesicles was analyzed by TEM.

3.2.3 Circular Dichroism (CD)

The CD was performed on a JASCO J-810 spectropolarimeter equipped with a PFD-425S Jasco temperature controller (Jasco, Inc., Easton, MD) in a quartz cuvette with a 1 mm path length. Scanning range was set between 190-260 nm at a rate of 100 nm/min with a 2 s response time and 2 nm bandwidth. Peptide: Lipid molar ratio was 1:16.5 with a 60 μM final concentration of MPX dissolved in 20 mM sodium phosphate buffer, 100 mM NaCl at pH 7.4.

3.2.4 Equilibrium Fluorescence

Fluorescence measurements were taken on a Flouromax spectrophotometer (Horiba Scientific, Edison, New Jersey). The 60 μM peptide samples dissolved in 20 mM sodium phosphate buffer at pH 6.4 before transfer to a 1 cm fluorescence cuvette. Data was collected using 3 nm excitation and emission slit width, exciting Trp at 280 nm with an integration time of 1 s over a total range of 285-550 nm.

3.2.5 Equlibrium Fourier Transform Infrared (FTIR) spectroscopy

The temperature dependent equilibrium FTIR experiments were carried out on a Varian 3100 Excalibur FTIR spectrophotometer coupled to a liquid nitrogen cooled mercury cadmium (MCT) detector. Samples were prepared in a split IR cell with an 126 μm Teflon spacer between two CaF_2 windows in a copper housing. Temperature dependent measurements were collected at 2 °C increments for both the reference (20mM sodium phosphate buffer, 100 mM NaCl, pH 7.4) and sample (16:1 d62-DPPC:MPX in

20 mM sodium phosphate buffer, 100 mM NaCl, pH 7.4). Each spectrum an average of 134 scans at 2 cm^{-1} resolution. MPX and LUVs were cooled mixed at 4 °C, prior to injection into the infrared cell.

3.2.6 Temperature-Jump Fluorescence Spectroscopy

The time-resolved T-jump apparatus used to measure peptide insertion and lipid relaxation in this study has been previously described. In this experiment, the pump beam is generated from a Ho:Nd YAG laser emitting light at 1908 nm. The pulsed emission at 50Hz is optically chopped to produce a 12.5 Hz repetition rate. A Verdi V12 DPSS high-power continuous wave laser (Coherent, Santa Clara, CA) is used to pump a Mira 900 Ti:Saph laser (Coherent) generating a 855 nm semi-continuous beam. The 285 nm excitation fluorescence probe beam is generated by passing the 855 nm beam through a second and third harmonic generator (Coherent). The back-emitted fluorescence light induced by the 285 nm pump laser is measured using a Hamamatsu R7518 photomultiplier tube (Hamamatsu Photonics K. K., Hamamat- su City, Japan), digitized, and signal averaged (4000 shots) using a Tektronics model 7612D digitizer. Instrument control and data collection are controlled using a LabVIEW computer program (National Instruments, Austin, TX). The same CaF_2 split IR cells used in the equilibrium FTIR measurements were used for the kinetic measurements. Deuterium exchanged MPX in $NaHPO_4$ buffer without membrane was used as the reference and internal thermometer to determine the final temperature and ultimate magnitude of the temperature-jump.

3.2.7 Time-Resolved Temperature Jump Infrared Spectroscopy

The time-resolved T-jump apparatus used to measure peptide insertion and lipid relaxation in this study has been previously described.[20,21] In this pump-probe method, 1.91 μm radiation serves as the pump beam in the rapid heating and subsequent perturbation of the system equilibrium. A tunable quantum cascade laser (Daylight Solutions, Inc., San Diego, CA) either in the 1525-1695 cm^{-1} for the peptide or the 2023-2145 cm^{-1} range for the lipids was used to probe the structural changes of the sample during the relaxation to a new equilibrium following the rapid temperature jump. The transmission changes in the IR probe beam are detected by a 200 MHz photovoltaic MCT detector (Kolmar Technologies, Newburyport, MA). The 1.91 μm (~35 mJ/pulse) pump beam is generated from a H_2 (g) filled Raman shifter (1 Stokes shift) pumped by a 10 Hz repetition rate Q-switched DCR-4 Nd:YAG laser (Spectra Physics, Mountain View, CA) and is absorbed by weak combination bands in the D_2O solution. The same CaF_2 split IR cells used in the equilibrium FTIR measurements were used for the kinetic measurements. The D_2O NaH_2PO_4 buffer contained in one of the compartments of the split IR cell serves as the internal thermometer to determine the final temperature and ultimate magnitude of the temperature-jump. The kinetic traces were generated by subtracting the change in absorbance of the reference at 1600 cm^{-1} from the 1650 cm^{-1} sample frequency of the lipid-peptide mixture in response to a temperature jump.

3.3 Results and Discussion

3.3.1 Characterization of MPX Folding by Circular Dichrosim (CD)

It has been previously reported that mastoparan X requires the presence of membranes to properly fold into an alpha-helical structure and can achieve folding in the presence of both anionic and zwitterionic membranes.[16,18] CD was used to confirm proper folding of the purified MPX and thermal stability in the presence of d62-DPPC

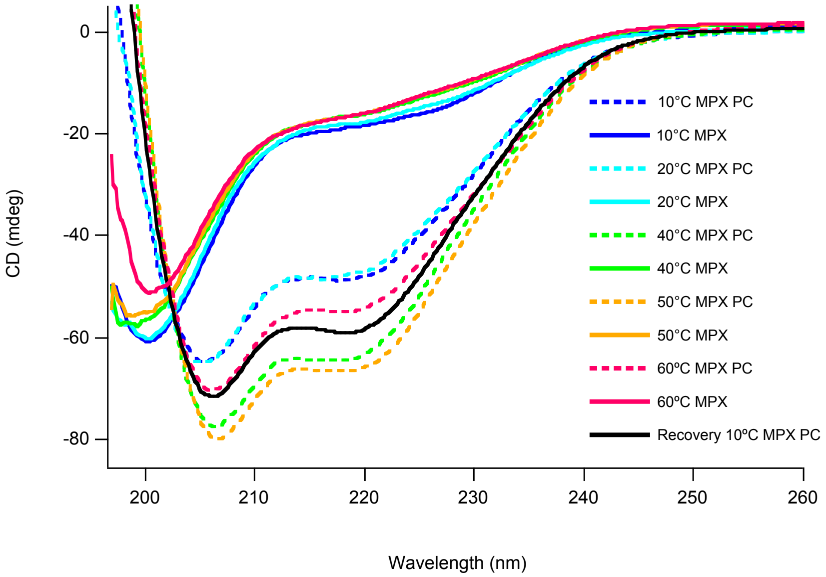

Figure 3.3. Characterization of MPX secondary structure by circular dichroism showing temperature dependent spectra of MPX with and without d62-DPPC membrane

membranes (Figure 3.3). The resulting spectra show that Mastoparan X adopts an unstructured conformation in aqueous media and folds into the expected alpha-helical conformation in the presence of d62-DPPC membrane vesicles, as evident by the helical bands revealing dual minima at 208 and 222 nm. In addition, the intensity of the 222 nm band is enhanced above the Tm of the membrane. This suggests an increase in helical content as the peptide inserts into the membrane. Further increase in temperature indicates a loss of intensity at 222 nm, suggesting that at higher temperatures MPX unfolds in the context of the membrane.

3.3.2 Membrane dependent MPX Fluorescence Emission

MPX contains an intrinsic tryptophan residue which provides a sensitive fluorescent probe where changes in solvation due to insertion causes an expected increase and blue shift in fluorescence intensity. Fluorescence intensity increases upon MPX association to the membrane, resulting in a dramatic increase and blue shift of fluorescence intensity from 346 nm to 327 nm (Figure 3.4). In addition, comparison of the integrated fluorescence intensity reflects band narrowing of MPX emission above the fluid phase transition of the membrane indicating the Trp residue is in a more homogenous environment in the membrane than in bulk solvent. The antimicrobial properties of MPX are derived from

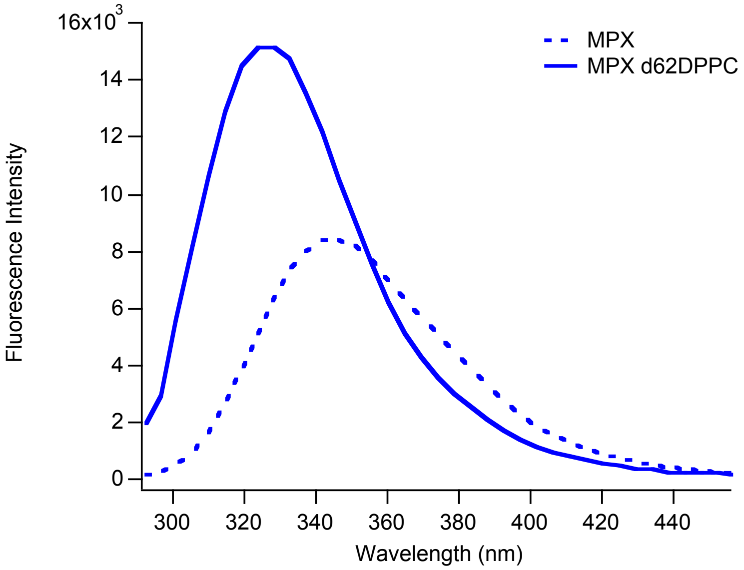

Figure 3.4. Fluorescence emission spectra of MPX with and without membrane

the ability of MPX to organize into pores once inserted into membranes.[22] A sulforhodamine B fluorescence leakage assay was performed to assess the effect of MPX insertion on membrane integrity (Summarized in Appendix Figure A3.1). From these results it is apparent that MPX does not induce leakage, at least on the timescale of these measurements.

3.3.3 Probing Peptide Insertion by Equilibrium FTIR

It has been well documented that the infrared absorbance of amide backbone of peptides are highly sensitive to changes in dielectric environment. Herein, we describe conversion of MPX from a solvated helix at the water-accessible membrane surface to a buried helix associated more closely associated with the hydrophobic membrane core. The temperature dependent equilibrium FTIR absorbance spectra show the temperature dependence of the peptide region primarily in the 1645 cm^{-1} region, the C=O of the ester moiety in the lipid head group around 1736 cm^{-1} and the CD_2 stretch making up the hydrophobic membrane core at 2088 cm^{-1} (Figure 3.5). Plotting the thermal transitions of the membrane reveals that introduction of the peptide to the membrane results in broadening of both the C=O and CD_2 transition determined by monitoring the spectral regions associated with lipid head group and the hydrophobic core at 1736 and 2088 cm^{-1}, respectively. In addition to broadening, the Tm of the d62-DPPC membranes is shifted from 37 °C to 32 °C in the presence of MPX, suggesting an interaction of MPX with the membrane involving both the headgroup of the lipids as well as the hydrophobic core. Since MPX inserts into disordered regions, e.g. at the plate interfaces of the model vesicles, it likely does not affect the ordered regions directly; however, it almost certainly increases the size of the disordered regions and by extension, decreases the size of the ordered ones. This ultimately leads to the observed decrease in the Tm, since the ordered domains are smaller and nucleation of the phase transition occurs more readily. To

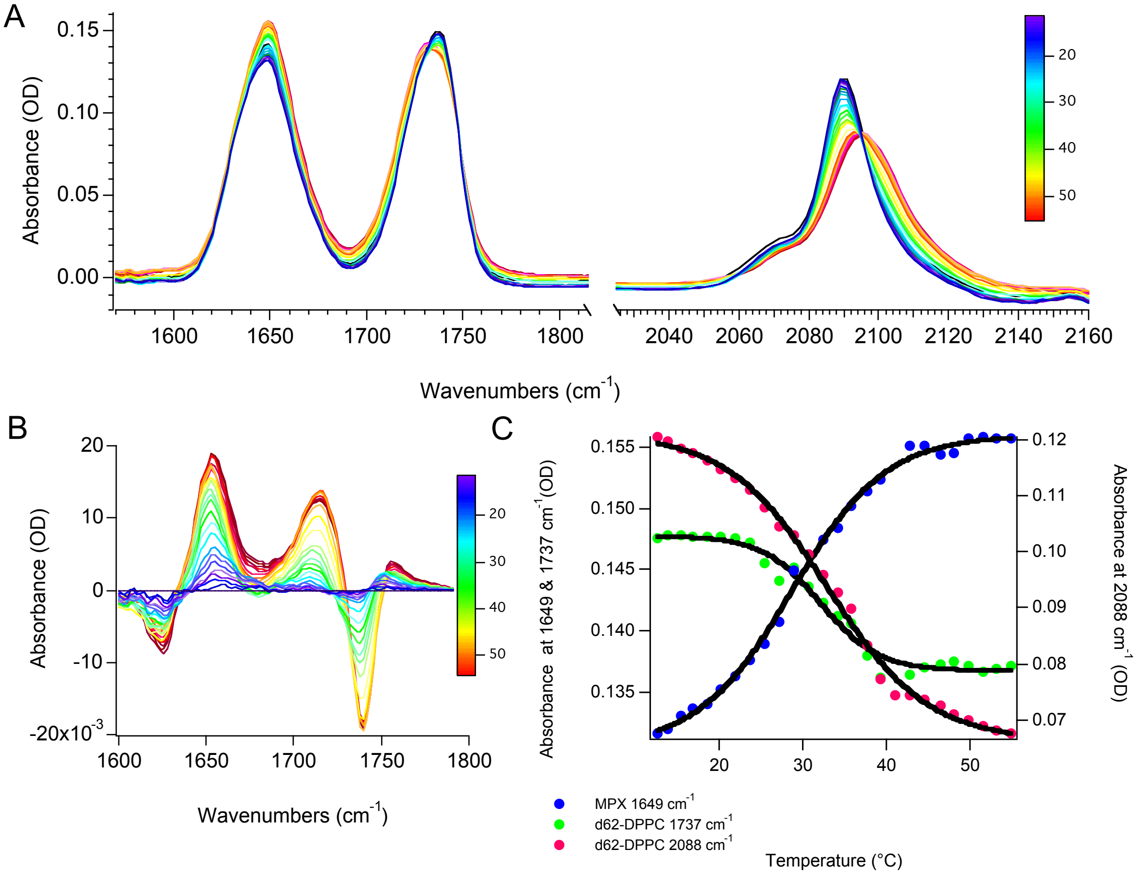

Figure 3.5. Equilibrium FTIR of MPX d62-DPPC (A) Temperature dependent raw absorbance spectra (B) FTIR difference spectra (C) Thermal melt curves

extract further detail involving changes in MPX in response to a temperature change, the difference spectra were generated. The FTIR difference spectra were generated by subtracting the lowest temperature spectrum at 10 °C from each of the higher temperature spectra. Analysis of the temperature dependent difference spectra reveal a bleach with a minimum centered at 1634 cm^{-1} and a maxima at 1655 cm^{-1}.

Previous studies have confirmed the 1634 cm^{-1} peak consistent with a solvated helix and the higher frequency 1655 cm^{-1} peak indicative of buried helix, consistent with MPX integrated into the membrane core. When the temperature is increased and the d62-DPPC vesicles enter the fluid phase transition, a clear bleach of the solvated helix, concomitant with the growth of the buried helix at 1655 cm^{-1} is observed, indicating the insertion of MpX promoted by the increasing degree of membrane fluidity. What is also apparent from the difference spectra is the disparity in the ratio between solvated and buried helix, where the distribution of buried helix is greatly favored. This discrepancy can be attributed to both a distribution in populations, as multiple equilibrium processes are occurring including peptide adsorption and desorption from the membrane, as well as insertion. Additional amplitude favoring the buried helix region may be a result of self-association of peptides within the membrane, as similar observations have been made with peptides known to generate helical bundles within the membrane,[23] e.g. bacteriorhodopsin. Additionally, re-cooling the sample to 10 °C post melt recovers only 78% of solvated helix amplitude, evidence that the insertion of MPX is not fully reversible. A two state process (insertion/de-insertion) should be completely reversible, thus, this result implies there is another process coupled to insertion. A likely candidate is aggregation, since this stabilizes the inserted structure, even in the gel phase of the membrane. Plotting the buried helix transition versus gel to fluid phase transition shows the midpoint of insertion occurring at approximately 5 degrees prior to the main transition of the membrane, suggesting that the membrane is not required to be completely in the fluid state, as MPX finds fluids defects in the membrane to insert well before the Tm of the membrane.

3.3.4. Time-resolved Temperature Fluorescence Spectroscopy.

Given our hypothesis that the kinetics of insertion are fast relative to association to the membrane and that insertion can be controlled by modulation of the fluid phase state, temperature-perturbing techniques again provide an ideal experimental platform for studying the dynamics and mechanism of MPX insertion. Fluorescence kinetic traces were generated by subtracting the change in emission of MPX without membrane in response to a t-jump, from emission generated from MPX in the presence of d62-DPPC. This subtraction is necessary to correct for the instantaneous loss of signal due to the temperature-dependent decrease in quantum yield of the Trp emission. The rate of insertion was determined by fitting the kinetic traces to a single exponential,

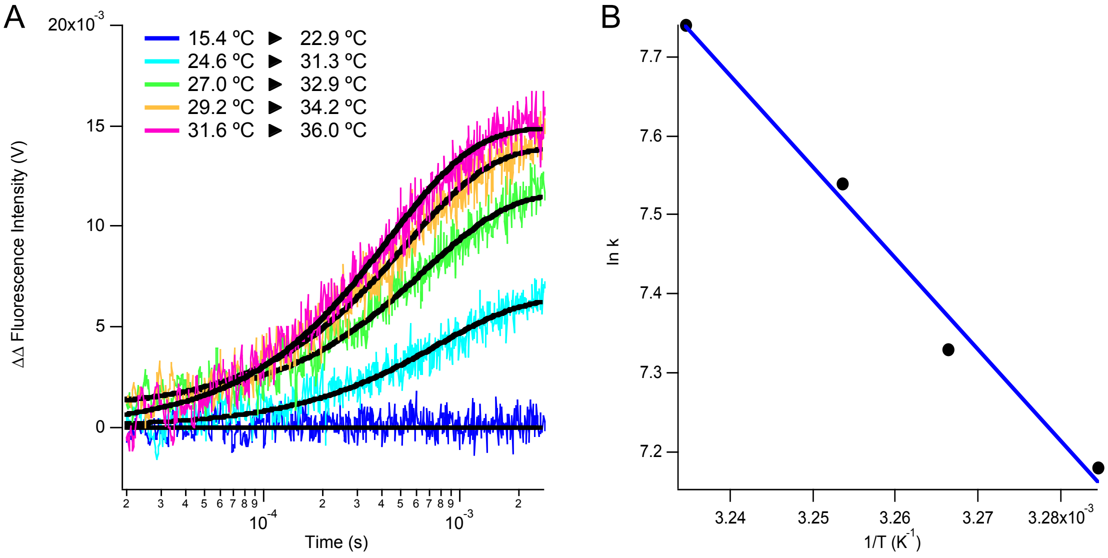

Figure 3.6. (A) T-jump Fluorescence spectra (B) Corresponding Arrhenius plot

T-Jump (°C)	**Tau(s)**
15.4-22.9	NA
24.6-31.3	$7.91e^{-4}$
27.0-32.9	$6.54e^{-4}$
29.2-34.2	$5.33e^{-4}$
31.6-36.0	$4.37e^{-4}$

Table 3.1. Summary of T-jump data in Figure 3.6

revealing burial of Trp into the membrane within a few hundreds of microseconds (Figure 3.6, Table 3.1). Insertion of MPX results in protection of the Trp residue from solvent quenching interactions,[24] thus generating a postive transient emission signal as observed in the t-jump fluorescence data. Arrhenius analysis of the resulting rates yielded a slope of -11542, corresponding to an apparent activation energy (Ea) of ~95 kJ/mol. No transient emission is observed for the first kinetic trace, corresponding to a jump from 15 °C to 22.9 °C. This observation is consistent with a model where MPX acquires entry into the membrane by insertion into defect sites or more fluid-like lipid consituency. When the d62-DPPC membrane is deep in the gel-phase, i.e. 15 °C, the highly organized, tightly packed lipid acyl chains exclude MPX from the hydrophobic core of the membrane. The apparent magnitude of transient emission is increased as the temperture-jump approaches the main transition of the membrane, correlating the increase of membrane fluidity with the degree of peptide insertion into the membrane.

3.3.5 Insertion Probed by Time-Resolved T-Jump Infrared Spectroscopy

To complement the T-jump fluorescence data, transition of the amide I’ backbone into the membrane was probed by T-jump infrared (TJIR). In this experiment, the buried helix band at 1650 cm^{-1} was used as the probe frequency to capture the dynamics of the amide I’ backbone as MPX inserts into model d62-DPPC vesicles. A frequency of 1600 cm^{-1} was selected as the reference because this region is associated with minimal signal from the amide backbone in the equilibrium FTIR measurements. Monitoring the 1650 cm^{-1} band reveals transient absorbance data that can be modeled to a biphasic fit, corresponding to 13 μs and 135 μs (Figure 3.7), and representing a temperature-jump from approximately 28 to 36°C. The first, faster phase is clearly observed in the TJIR experiments, but not observed in the transient fluorescence data, indicating that this phase is unique to the amide transition. This phase may be attributed to rearrangement of the amphiphilic helix on the surface of the membrane as the peptide achieves insertion.

The second, slower phase of the transient absorption data harbors the majority of the amplitude and thus is the major reporter on insertion. This phase corresponds to the transient data observed in the t-jump fluorescence data. Interestingly, the observed rate is approximately two to three times faster than the rate observed in the transient fluorescence experiments. In this instance, tryptophan is a local probe and senses insertion near the N-terminus. In contrast, the IR probe is the helix component of amide I’ band, which reports on the global backbone. Therefore, the IR transient gives an average rate of burial of the entire helix. This is faster than the burial of the N terminus, indicating highly directional insertion. The difference in rates between the transient infrared and fluorescence data also suggest that insertion may be achieved gradually or quite possibly, in a step-wise fashion.

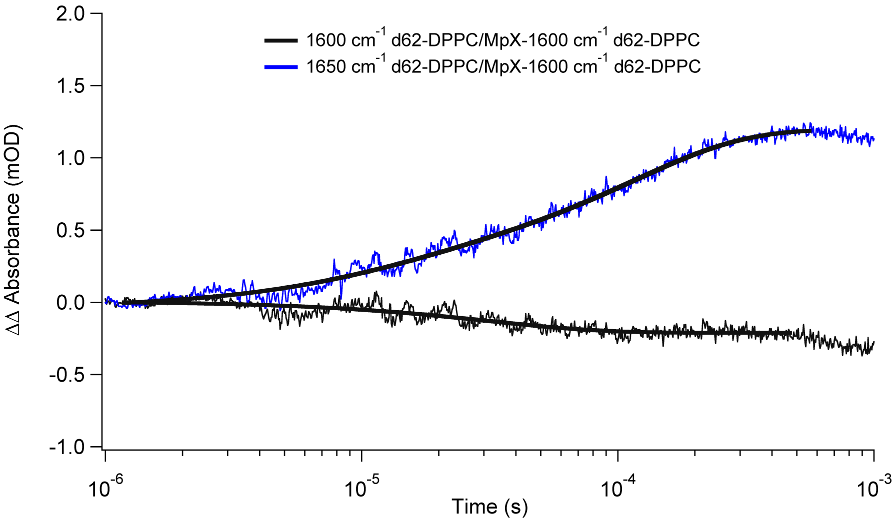

Figure 3.7. T-jump IR spectra (blue) buried helix transition (black) reference wavelength

T-Jump infrared spectroscopy also lends itself to probing the dynamics of the d62-DPPC membrane during insertion of MPX. Transient absorbance data was plotted versus time and fit to a stretched exponential function, where the B term indicates deviation from a classic exponential function, i.e. B=1 represents an exponential fit:

$$f(x) = y0 + A1 * \exp\left(-\frac{x-x0}{tau1}\right) + A2 * \exp\left(-\left(\frac{x-x0}{tau2}\right)^{B1}\right) \qquad \text{(Eq.3.1)}$$

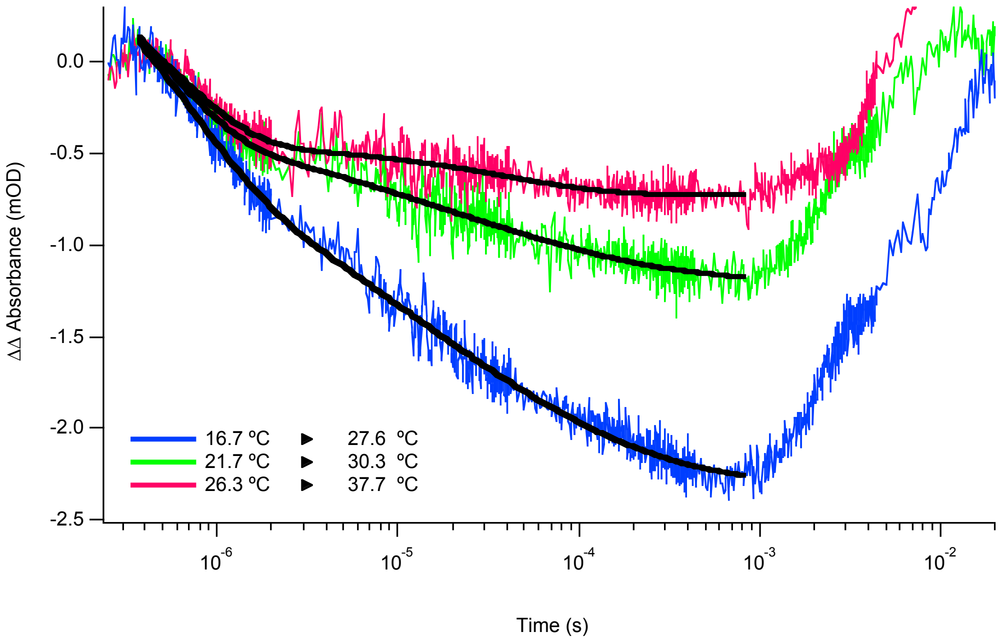

Figure 3.8. T-jump IR of d62-DPPC membranes in the presence of MPX

T-jump (°C)	**Fast Phase (s)**	**Slow Phase (s)**	**B**
16.7-27.6	7.20e e^{-7}	1.11 e^{-5}	0.322
21.7-30.3	5.00 e^{-7}	1.60 e^{-5}	0.346
26.3-37.7	6.22 e^{-7}	3.83 e^{-5}	0.717

Table 3.2. Summary of T-jump IR data in Figure 3.7

Transient absorbance data shows little perturbation of lipid dynamics in the presence of MPX relative to those observed in Chapter 2 (Figure 3.8, Table 3.2). However, the relative amplitude of the fast to slow phase is decreased, which can be justified by loss of membrane order due to the incorporation of MPX. Since the slow phase represents the slow propagation of the phase transition as pressure builds up within the bilayer, the difference in amplitudes with MPX present suggests the membrane is less able to accommodate the buildup of this pressure, and also perhaps the equilibration of water across the membrane is slower. These findings are consistent with the observation that the presence of MPX did not induce membrane leakage, and also suggests that the more crowded environment slows down the transition, although not enough to prevent MPX insertion.

3.4 Conclusions

Using temperature-jump infrared and fluorescence spectroscopy we determined the rate of MPX insertion into d62-DPPC lipid vesicles. This experiment was executed by utilizing the rigid features of saturated membranes to allow for accumulation of solvated MPX on the membrane surface. MPX insertion was then triggered by thermal control of the fluid phase transition of the d62-DPPC vesicle. As a result, we have characterized the insertion of MPX as a biphasic kinetic process, both of which are resolved in the T-jump infrared experiment. The faster, 13 μs rate may be attributed to a rearrangement of the amphiphilic helix on the membrane surface, where the slower rate at 135 μs corresponds to the primary insertion event signifying bulk dehydration of the amide backbone. The fluorescence T-jump studies probing the intrinsic tryptophan residue indicate only one kinetic event, hundreds of microseconds slower than the primary infrared transient event. Taken together, these results suggest that insertion of MPX is highly directional and is directed by the C-terminus of the peptide. In addition, both the equilibrium and transient experiments are consistent with the observation that propagation of MPX insertion is enhanced by an increase in membrane fluidity.

The results detailed in this chapter indicate that the rate of MPX insertion is an order of magnitude faster than previous reports identifying this process on the millisecond timescale. This discrepancy in observed rates is due to experimental limitations of methods previously used to study the dynamics of insertion, as stopped-flow kinetics are limited by both time resolution, i.e. late microsecond to millisecond timescales, and diffusion rates of the peptide and membrane. The methodology presented in this chapter is a significant improvement on experimental approaches formerly used to study protein insertion. Transient measurements acquired by temperature-jump provide a significant enhancement in time resolution (tens of nanoseconds to milliseconds), while simultaneously providing a trigger to thermally induce the gel to fluid phase transformation of the membrane, thereby promoting MPX insertion. The ability to selectively control membrane rigidity and therefore, permeability allows for equilibration of the peptide with the membrane surface, avoiding experimental limitations consequence of diffusion and/or mixing time. The data presented herein also defines the thermodynamic parameters governing MPX insertion. Arrhenius analysis of the determined rate constants for insertion reveals an activation energy of 95 kJ/mol. This value is quite high relative to typical energies observed for processes such as protein folding, e.g. 20-60 kJ/mol. This large barrier likely has contributions from the fluid phase transition of the membrane which requires ~62 kJ/mol,[24] de-solvation of the amide backbone upon burial of MPX into the membrane, and quiet possibly continued folding of the structure upon insertion. Comparison of the rate of the d62-DPPC fluid phase transformation to burial of MPX suggests that insertion of MPX is on a competitive timescale with full thermal relaxation of the lipid vesicles. Taken together, these experiments allow for greater mechanistic insight into the dynamic interplay between membranes and proteins.

3.5. References

1. Martens, S. and McMahon, H. T. Mechanisms of membrane fusion: disparate players and common principles Nature Reviews Molecular Cell Biology. 2008, 9, 543-556.

2. Cymer, F., von Heijne, G., White, S. H. Mechanisms of Integral Membrane Protein Insertion and Folding J. Molec. Biol. 2015, 427(5), 999-1022.

3. Lorenz, D., Wiesner, B., Zipper, J., Winkler, A., Krause, E., Beyermann, M. Lindau, M., Bienert, M. Mechanism of Peptide-induced Mast Cell Degranulation Translocation and Patch-Clamp Studies. JGP. 1998, 112(5), 577-591.

4. Munnik, T., Arisz, S.A., De Vrije, T. and Musgrave, A. G Protein Activation Stimulates Phospholipase D Signaling in Plants.The Plant Cell. 1995 7(12), 2197-2210.

5. Carr, C. M., and Kim, P.S. A spring-loaded mechanism for the conformational change of influenza hemagglutinin. Cell. 1993, 73(4), 823-832.

6. Fidai S., Farmer S.W., Hancock R.E. Interaction of cationic peptides with bacterial membranes. Methods Mol. Biol. 1997, 78, 187–204.

7. Niyonsaba F., Nagaoka I., Ogawa H., Okumura K. Multifunctional antimicrobial proteins and peptides: Natural activators of immune systems. Curr. Pharm. Des. 2009, 15, 2393–2413.

8. Koczulla A.R., Bals R. Antimicrobial peptides: Current status and therapeutic potential. Drugs. 2003, 63, 389–406.

9. Otvos L., Jr Antibacterial peptides and proteins with multiple cellular targets. J. Pept. Sci. 2005, 11, 697–706.

10. Galdiero S., Falanga A., Tarallo R., Russo L., Galdiero E., Cantisani M., Morelli G., Galdiero M. Peptide inhibitors against herpes simplex virus infections. J. Pept. Sci. 2013, 19, 148–158.

11. Hancock R.E. Cationic peptides: Effectors in innate immunity and novel antimicrobials. Lancet Infect. Dis. 2001, 1, 156–164.

12. Tossi A., Sandri L., Giangaspero A. Amphipathic, alpha-helical antimicrobial peptides. Biopolymers. 2000, 55, 4–30.

13. Lehrer R.I., Ganz T. Antimicrobial peptides in mammalian and insect host defence. Curr. Opin. Immunol. 1999, 11, 23–27.

14. Fox, J. L., Antimicrobials stage a comeback. Nat. Biotechnol. 2013, 31, 379–382.

15. Hancock, R. E. W., and Sahl, H-G. Antimicrobial and host-defense peptides as new anti-infective therapeutic strategies. Nature Biotechnology. 2006, 24, 1551 – 1557.

16. Sitaram, N. and Nagaraj, R. Interaction of antimicrobial peptides with biological and model membranes: structural and charge requirements for activity Biochimica et Biophysica Acta: Biomembranes. 1999, 1462(1-2), 29-54.

17. Higashijima T, Uzu S, Nakajima T, Ross EM (May 1988). Mastoparan, a peptide toxin from wasp venom, mimics receptors by activating GTP-binding regulatory proteins (G proteins). J. Biol. Chem. 1988, 263 (14), 6491–64914.

18. Asakura, T. et al. Interaction of mastoparan with membranes studied by ^{1}H-NMR spectroscopy in detergent micelles and by solid-state ^{2}H-NMR and ^{15}N-NMR spectroscopy in oriented lipid bilayers. Eur. J. Biochem. 2001, 268, 302-309.

19. Role of Helix Nucleation in the Kinetics of Binding of Mastoparan X to Phospholipid Bilayers. Biochemistry, 2007, 46 (48), 13856–13863.

20. Dyer, R. B., Gai, F., Woodruff, W. H., Gilmanshin, R., Callender, R. H. Infrared Studies of Fast Events in Protein Folding. Acc. Chem. Res. 1998, 31, 709-716.

21. Williams, s., Causgrove, T. P., Gilanshin, R., Callender, R. H., Woodruff, W. H., Dyer, R. B. Fast Events in Protein Folding: Helix Melting and Formation in a Small Peptide. Biochemistry. 1996, 35, 691-697.

22. Arbuzova, A., Schwarz, G. Pore-forming action of mastoparan peptides on liposomes: a quantitative analysis. Biochim Biophys Acta. 1999, 1420(1-2), 139-52.

23. Rath, P., Bousch, O., Meril, A. R., Cramer, W. A., Rothschild, K. J. Fourier transform infrared evidence for a predominately alpha-helical structure of the membrane bound channel forming COOH-terminal peptide of colicin El. Biophysical Journal 1991, 59, 516-522.

23. Eftink, M. R., Ghiron, C. A. Exposure of tryptophanyl residues and protein dynamics. Biochemistry, 1977,16 (25), 5546–5551.

24. Nagarajan, S., Schuler, E. E., Ma, K., Kindt, J. T., and Dyer, R. B. Dynamics of the Gel to Fluid Phase Transformation in Unilamellar DPPC Vesicles. J Phys. Chem. B. 2012, 116 (46), 13749-13756.

25. Arbuzova, A. and Schwarz, G. Pore-forming action of mastoparan peptides on liposomes: a quantitative analysis. BBA: Biomembranes. 1999, 1420(1-2), 139-152.

Appendix 3: Insertion of Mastoparan X into Model d62-DPPC Lipid Vesicles Triggered by Rapid Thermal Initiation of the Membrane Phase Transition

A3.1 Sulforhodamine B Leakage Assay

Previous studies indicate that association of multiple MPX peptides promotes pore formation in small unilamellar vesicles.[25] However, at approximately 2.1 nm in length (folded), MPX cannot completely span the 4.2 nm d62-DPPC bilayer. We hypothesize that formation of well-defined pores in the membrane should have a dramatic effect on the properties of the membrane. To initially test the possibility of pore formation within the membrane, a leakage assay was performed where sulforhodamine B was encapsulated in the d62-DPPC lipid vesicles at a self-quenching concentration.

Samples were prepared by adding a saturated solution of sulforhodamine B to a dried lipid film as the hydration media, thereby encapsulating the quenched dye within the membrane structure. Extrusion of the lipids resulting in the LUVs was carried out as described above previously. Excess dye was removed from the exterior of the vesicle solution by gravity drip size exclusion chromatography using a sephadex G-25 column (GE Life Sciences). As a control, the temperature dependent decay in fluorescence for vesicles with sulforhodamine B encapsulated was assessed. The temperature was adjusted from 15 °C to 50 °C to assess basal leakage of the membrane without MPX present. At the final temperature, the sample was spiked with a concentrated solution (~300 μM) Tween 20 detergent to induce leakage, resulting in dilution of sulforhodamine B and an increase in fluorescence intensity centered at the emission maximum of 589 nm. To determine the effect of MPX on membrane integrity, a fresh solution of sulforhodamine B encapsulated vesicles was prepared with the addition of MPX. The same temperature titration was completed. Again, Tween 20 detergent was added at the last temperature to induce leakage. These results indicate little deviation between vesicle solution with and without MPX. Importantly, there is no discontinuity in fluorescence emission going through the phase transition of the membrane and addition of a surfactant at the end of

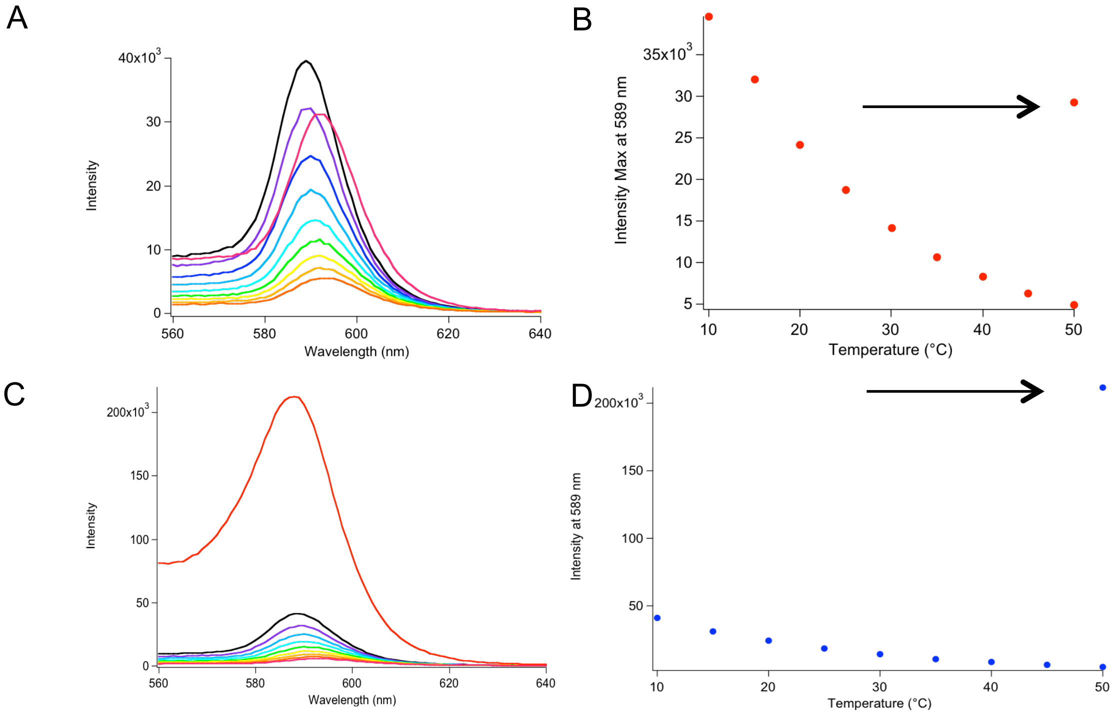

Figure A3.1 Sulforhodamine B leakage assay (A) Fluorescence emission of dye encapsulated vesicles only (B) Plot of max intensity for data shown in (A) at 585 nm (C) Fluorescence emission of dye encapsulated vesicles in the presence of MPX (D) Plot of max intensity for data shown in (C) at 585 nm. Black arrows in (B) and (D) indicate addition of surfactant.

the temperature titration results in a large increase in fluorescence, clear evidence that the dye is not liberated from the vesicles until the membranes are intentionally disrupted in the presence of Tween 20. These results suggest that the integrity of the d62-DPPC membranes was not compromised upon addition of MPX on the timescale of this experiment. While insertion of MPX may result in significant thinning of the membrane there was no clear indication of pore formation or that the overall integrity of the membrane was compromised on the timescale of these experiments (hrs).

Chapter 4: Characterization of the Folding Dynamics of Hemagglutinin HA2 L40 peptide

4.1 Introduction

The influenza virus is responsible for three major pandemics from the 19th century to present day.[1,2] This virus remains an elusive target to therapeutics and prophylactic treatments such as vaccines due to its ability to rapidly mutate, rendering even the most promising treatments ineffective.[3,4,5] Understanding the basis of influenza pathogenicity well enough to generate effective therapeutics requires intimate knowledge of viral components responsible for infectivity. Importantly, it is widely hypothesized that the mechanistic underpinnings of influenza are conserved through many classes of viruses,[6] further bolstering the importance of studying the fundamental aspects of viral structures.

4.1.1 Hemagglutinin Structure and Function

Influenza harbors three major viral coat proteins within its membrane.[7] One of these proteins, hemagglutinin (HA), plays a major role in influenza infectivity by participating in both recognition of viable host cells and membrane fusion, which promotes release of viral genetic components after viral uptake into host cells. [8] Hemagglutinin exists as a functional trimer within the influenza virus. HA is composed of two domains. The first, HA1, is responsible for recognition and docking of the virus onto the host cell. The second, HA2, harbors the fusion peptide and pH sensitive trigger.[8,9]

Hemagglutinin first initiates viral infectivity through recognition of sialic acid moieties on the membrane surface of host cells.[7,10] After docking on the host cell, the influenza virus is taken into the host through endocytosis.[11] In an effort to digest the contents of the endosome, the endosome is acidified. Influenza is opportunistic, in that it uses the drop in pH to activate HA, which undergoes a dramatic conformational rearrangement, liberating the fusion peptide and extending its structure over 100 °A to present the HA fusion peptide to the inner endosomal membrane.[9] After insertion of the fusion peptide in the host membrane, HA protein undergoes a second conformational rearrangement, ultimately drawing the viral and host membranes together.[11] In this process the HA transmembrane domain interacts with the fusion peptide, creating the HA fusion pore. This general mechanism ultimately leads to complete fusion of the viral and host membranes, and is a pathway for viral RNPs to enter the host cell.

4.1.2 Models of HA Folding

The earliest and most widely accepted model describing the mechanism of HA is the "spring-loaded" mechanism put forth by Kim and coworkers.[9,12] This mechanistic interpretation of the structural changes dictating HA function describes the symmetric extension of the HA towards the host membrane facilitated by the pH driven folding of a loop that is otherwise unstructured in the neutral HA structure. More recently, additional theoretical models have been put forth describing alternate pathways to achieve HA extension leading to insertion and fusion. These models include the cooperative and sequential model, which mainly differ from the spring loaded mechanism by the order of presumed events and that both models describe asymmetric extension of HA components to generate the low pH structure. [13]

4.1.3 Loop-40 Coiled-coil

Perhaps one of the most critical components of the HA mechanism is the ability of HA to respond to endosomal acidification, as this response yields both liberation of the fusion peptide and extension of the structure promoting access of the fusion peptide to the host membrane for insertion. Early analysis of the HA primary sequence revealed a stretch of HA containing a dense distribution of glutamic acid residues. It is postulated that at neutral pH, the glutamic acid residues apart of this loop are charged, but upon acidification of the endosome, these acidic residues are protonated, charge repulsion is relieved and the loop folds into an alpha helical moiety[9,12,14] (Figure 4.1). We will refer to this pH trigger as the Loop-40 peptide (L40) (Figure 4.1 B). Association with the helices from neighboring components of the trimer results in an extended parallel, trimeric coiled-coil motif, stabilized by hydrophobic interactions.[14,15] Further evidence for this model is supported by

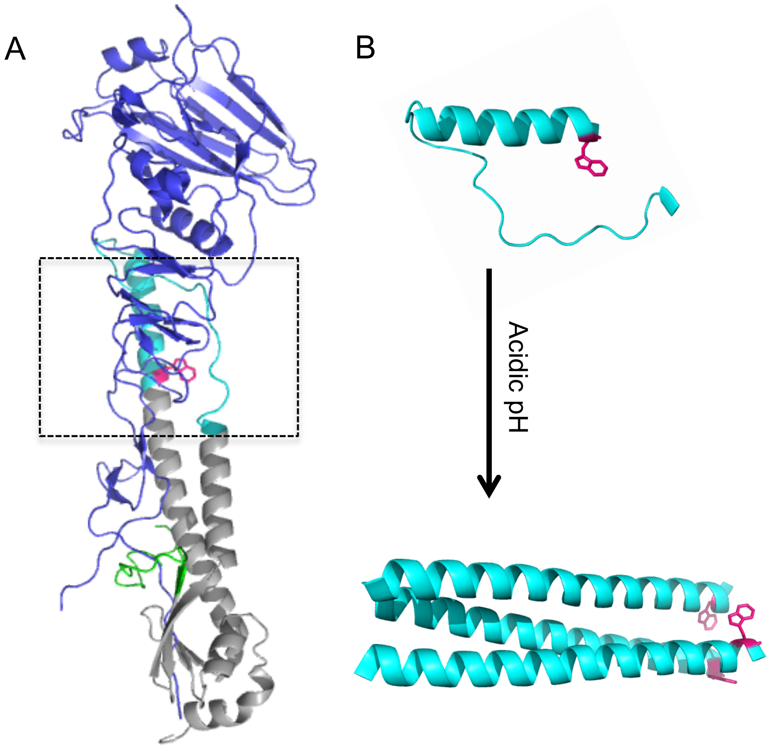

Figure 4.1. (A) Neutral pH structure of the HA monomeric ectodomain (transmembrane domains not shown, PDB: 2HMG and 1HTM), showing: HA1 domain (purple) and HA2 domain (teal and grey) the fusion peptide is a part of the HA2 structure and is shown in green (B) pH response of the acidic L40 peptide corresponding to the black box in (A)

the x-ray crystal structures attained at neutral and acidic pH, suggesting that formation of the L40 coiled coil motif is critical to downstream events in the HA mechanism, especially insertion of FP into the host membrane.

In general, coiled-coil motifs are a prolific structure and have been associated with a number of important biological functions and material applications. Studies based on sequence analysis predict that 2-5% of all proteins contain a coiled-coil motif. [16] Furthermore, many vital biological processes require assembly of coiled-coil motifs, such as the SNARE superfamily of proteins, regulating vesicle fusion to target membranes,[17] GCN4, regulating eukaryotic transcriptional activation,[18] and HAMP domains, which play a critical role in bacterial sensing and chemotaxis.[19] Coiled-coil motifs are also quite prolific in other viral fusion processes, with examples beyond HA including Ebola GP2 and HIV gp41.[20, 21] Intriguingly both these examples are functional as trimeric structures.

Coiled-coil proteins have previously been characterized by a number a equilibrium methods and to a lesser extent, subjected to dynamic folding studies with temperature-jump infrared and pH jump spectroscopy using caged photo-acids. [22, 23, 24] Although thought to be a critical component of the HA mechanism, there are still many questions regarding the dynamics governing folding of the L40 coiled-coil. For example, what is the timescale of folding? What thermodynamic barriers are overcome to achieve formation of the coiled-coil trimer? What is the role of protonation of the glutamic acid residues? What intermediates are utilized on the folding pathway to the final structure? This chapter interrogates the folding mechanism of HA L40 trimer. These results will aid in validating experimental models for HA folding and add to our general understanding of protein mediated viral fusion.

4.2 Materials and Methods

4.2.1 Peptide Synthesis and Purification

L40 F63W F70W W92F peptide: RVIEKTNEKWHQIEKEWSEVEGRIQDLEKYVEDTKIDLFS and variants (WT, L40 F63W W92F, L40 F70W W92F) described in this study were synthesized by standard Fmoc solid phase peptide synthesis utilizing acid-amine coupling on a Liberty 1 peptide synthesizer (CEM, Matthews, NC) using a rink-amide resin. Fmoc protected amino acids were purchased from AnaSpec, Inc. (Fremont, CA) Purification of L40 peptide was completed on a reverse phase C18 column (Phenomenex, Torrance, CA) with TFA as a counterion using a linear gradient of water and acetonitrile. The mass of the purified peptide was confirmed by MALDI-MS using CHCA matrix dissolved in 50:50 mixture of water: acetonitrile. MS confirmed presence of L40 WT and L40 F63W F70W W92F with masses equal to 4909 and 4949 amu, respectively. The peptide was then subjected to two cycles of acid exchange in 20 mM solution of HCl to remove TFA for FTIR experiments.

4.2.2. Circular Dichroism

The secondary structure of L40 peptide was confirmed by circular dichroism (CD). CD was performed on a JASCO J-810 spectropolarimeter equipped with a PFD-425S Jasco temperature controller (Jasco, Inc., Easton, MD). The peptide was dissolved in water and adjusted to pH 4.8 or pH 7.0 at a 60 μM final peptide concentration. The samples were transferred to a quartz cuvette with a 1 mm path length. The scanning range of the instrument was set between 190-260 nm at a rate of 100 nm/min with a 2 s response time and 2 nm bandwidth. Temperature dependent data was collected in 2 °C increments monitoring 222 nm wavelength.

4.2.3 Analytical Ultracentrifugation

The AUC and analysis described herein was performed in collaboration with the Center for Analytical Ultracentrifugation of Macromolecular Assemblies (San Antonio, TX) on a Beckman Optima XL-A/I AUC (Beckman Coulter, Indianapolis, IN). The AUC was preformed on four samples, representing two different pH values at 4.45 and pH 7.04 and two concentrations for each pH corresponding to an optical density of 0.3 and 0.9 at 280 nm. A plot of sedimentation velocity coefficient $s_{20,w}$ versus signal concentration reveal two distinct distributions corresponding to a sedimentation coefficients of ~0.9 and ~1.9, for the pH 7 and pH 4 samples, respectively.

4.2.4 Fluorescence Emission

Fluorescence measurements were taken on a Flouromax spectrophotometer (Horiba Scientific, Edison, New Jersey). The 60 μM peptide samples were adjusted to pH 4 or pH 7, before transfering to a 1 cm fluorescence cuvette. Data was collected using 3 nm excitation and emission slit widths, exciting Trp at 280 nm with an integration time of 1 s over a total range of 285-550 nm.

4. 2.5 Equilibrium FTIR

The temperature dependent equilibrium FTIR experiments were carried out on a Varian 3100 Excalibur FTIR spectrophotometer coupled to a liquid nitrogen cooled mercury cadmium (MCT) detector. Samples were prepared in a split IR cell with a 126 μm Teflon spacer between two CaF_2 windows in a copper housing. Temperature dependent measurements were collected at 2 °C increments for both D_2O reference and L40 sample at pH 4. Each spectrum is an average of 134 scans at 2 cm^{-1} resolution. Temperature dependent absorbance spectra yield a helical band centered at 1645 cm^{-1}.

4.2.6 Temperature-Jump Infrared Spectroscopy

The time-resolved T-jump apparatus used to measure peptide insertion and lipid relaxation in this study has been previously described.[25,26] In this pump-probe method, 1908 nm radiation serves as the pump beam in the rapid heating and subsequent perturbation of the system equilibrium. A quantum cascade laser (Daylight Solutions, Inc., San Diego, CA) with a tunable range from 1525-1695 cm^{-1} was used to probe the structural changes of the peptide during the relaxation to a new equilibrium following the rapid temperature jump. The transmission changes in the IR probe beam are detected by a 200 MHz photovoltaic MCT detector (Kolmar Technologies, Newburyport, MA). The 1908 nm pump beam at a ~12.5Hz repetition rate is generated from a Q-switched Ho:YAG laser emitting at 50Hz and is passed through an optical chopper (Thor Labs, Newton, NJ) to achieve the 12.5 Hz repetition rate. The pump beam is absorbed by weak combination bands in the D_2O solution. The same CaF_2 split IR cells used in the equilibrium FTIR measurements were used for the kinetic measurements. The D_2O on one side of the split IR cells serves as the reference and internal thermometer to determine the final temperature and ultimate magnitude of the temperature-jump. The kinetic traces were generated by subtracting the change in absorbance of the D_2O reference from that of the lipid-peptide sample in response to the temperature jump.

4.2.7 Temperature Jump Fluorescence Spectroscopy

The time-resolved T-jump apparatus used to measure peptide insertion and lipid relaxation in this study has been previously described. In this experiment a Ho:Nd YAG emitting generating 50 Hz pulsed emission is passed through an optical chopper (Thor Labs, Newton, NJ) to a 12.5Hz repetition rate. A Verdi V12 DPSS high-power continuous wave laser (Coherent, Santa Clara, CA) is used to pump a Mira 900 Ti:Saph laser (Coherent) generating a 855 nm semi-continuous beam. The 285 nm excitation fluorescence probe beam is generated by passing the 855 nm beam through a second and third harmonic generator (Coherent). The emitted fluorescence light induced by the 285 nm pump laser is measured using a Hamamatsu R7518 photomultiplier tube (Hamamatsu Photonics K. K., Hamamatsu City, Japan), digitized, and signal averaged (4000 shots) using a Tektronics model 7612D digitizer. Instrument control and data collection are controlled using a LabVIEW computer program (National Instruments, Austin, TX). The same split cell in copper housing used in the infrared experiments was used for the transient fluorescence measurements. The cell was prepared using a 126 μm spacer. A solution of free Trp dissolved in D_2O is used to determine the temperature jump and determine the temperature dependence of the tryptophan signal. The L40 peptide sample was prepared by dissolving 75 μm of lyophilized D_2O exchanged L40 peptide in D_2O at a final concentration of 75 μm and adjusting the pH of sample to a desirable range between pH 4-4.8.

4.3 Results and Discussion

4.3.1 Characterization of Secondary Structure by Circular Dichroism

Circular dichroism was performed in order to determine proper folding of the L40 derivative analyzed in this study, into the expected alpha-helical secondary structure. CD spectra indicate unfolded peptide at neutral pH and alpha helical structure at low pH (Figure 4.2A). The models for a number of pH sensitive coiled-coil motifs typically attribute folding to protonation of acidic residues in the peptide sequence, and in this instance, the dense distribution of glutamic acid residues. Neutralizing the charge on the acidic residues screens repulsive interactions allowing the peptide to assume a helical conformation.[27] Further oligomerization of the helices is driven mostly by favorable hydrophobic contacts.[14, 15] Temperature dependent data was collected every 2 °C. The resulting curve was fit to a sigmoid and yields a Tm of 47.8 °C for L40 F63W F70W F92F (Figure 4.2 B-C). The ratio of the n-π* at 222 nm to π - π *208 nm has previously been used to characterize helical oligomers derived from HA structure.[28, 29] In this qualitative analysis, comparison of CD intensities at 222/208 nm indicate the presence of helical oligomers at values greater than 0.86.

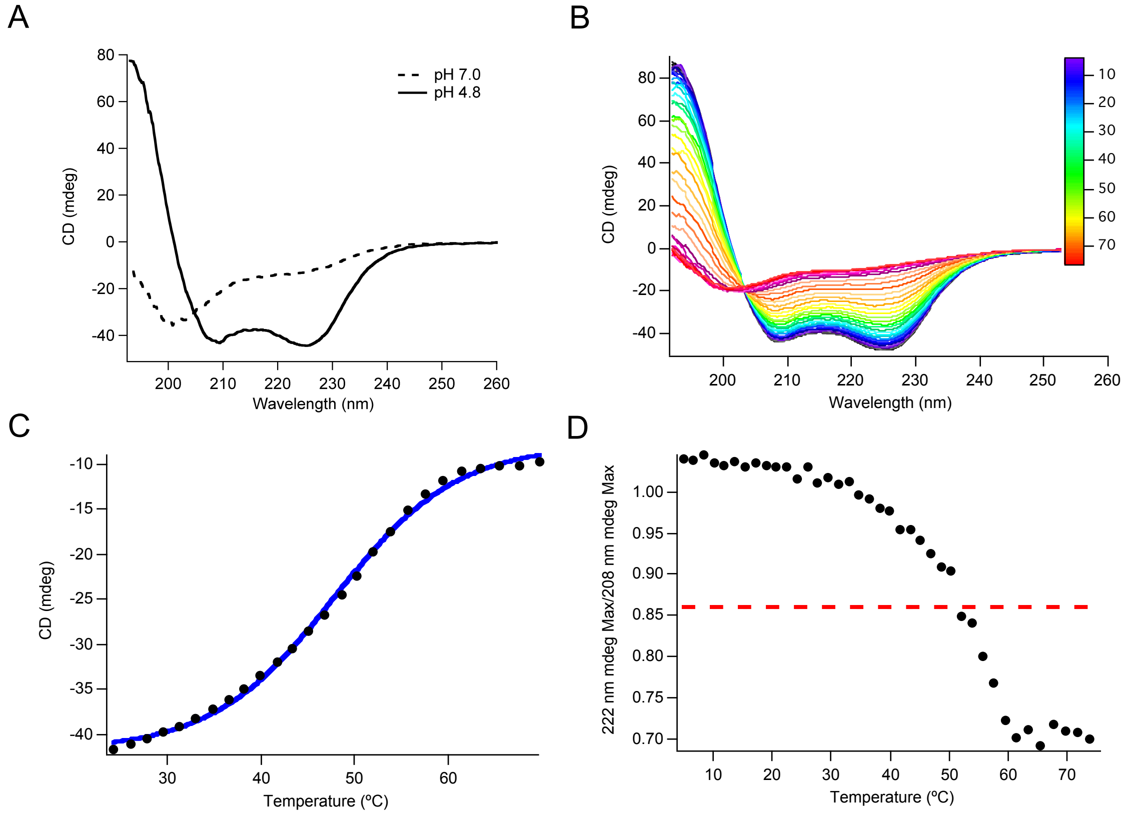

Figure 4.2 Secondary structure characterization by circular dichroism (A) pH dependent folding of L40 peptide (B) Temperature dependent CD Melt data, spectra collected every 2°C (C) Thermal melt curve monitoring 222 nm transition (D) Temperature dependent ratio n-π* at 222 nm/π - π *208 nm.

The CD data herein indicates a 222/208 nm ratio consistent with the presence of an oligomer up to ~52 ºC (Figure 4.2 D). Together, these data are consistent with the expectation that the pH induced folding of L40 F63W F70W F92F will oligomerize into a trimeric coiled-coil structure.

4.3.2 Analytical Ultracentrifugation

Perhaps the most quantitative analysis validating trimer assembly for the L40 F63W F70W F92F peptide is structural confirmation by Analytical Ultracentrifugation (AUC). AUC is a highly quantitative method that measures progression of a macromolecular concentration boundary from the meniscus of a sample that is subjected to centrifugal force. The metric for interpreting AUC is the sedimentation velocity coefficient, s, which typically is expressed in Svedburg units, (S), i.e. 10^{-13} sec. The Svedberg equation defines the sedimentation coefficient as (Eq. 1):[30,31]

$$s = \frac{u}{\omega^2 r} = \frac{M(1-\bar{v}p)}{N_a f} = \frac{MD(1-\bar{v}p)}{RT}$$

Where, u is the experimentally observed radial velocity of the protein or macromolecule studied, ω is the angular velocity of the rotor, $\omega^2 r$ is the centrifugal field, M is the molar mass, $\bar{v}$ represents the partial specific volume, ρ is the density of the solvent, N_A is Avagadro's number, f represents the frictional coefficient, which is effectively a measure of how globular the protein is, i.e anisotropy, D is the diffusion coefficient, and finally R is the ideal gas constant.

In order to determine the upper limit of s for a macromolecule of a given mass, the Stokes equation is used to calculate the frictional coefficient of an ideal spherical protein (Eq. 2):[30]

$$f_0 = 6\pi\eta R_0$$

Where, η is the viscosity and R_0 is the radius of the sphere. R_0 may also be expressed as (Eq. 3):[30]

$$R_{0\,sphere} = \left(\frac{3M\bar{v}}{4\pi N_A}\right)^{1/3}$$

Combining the Svedburg and Stokes equations and substituting constant values for water at 20 °C yields the reduced equation (Eq. 4):[30]

$$s_{sphere} = 0.012\frac{M^{2/3}(1-\bar{v}p)}{\bar{v}^{1/3}}$$

This equation can be used to determine s values for ideal spheres of a given mass. In essence, this value represents the *theoretical maximum s* value attainable and therefore corresponds to the *minimal frictional coefficient* f_0.[32] Experimentally determined s values are subjected to an additional correction factor such that sedimentation velocity coefficients are normalized to standard conditions, denoted $s_{20,w}$ in the following equation (Eq. 5):[30]

$$s_{20,w} = s_{T,B}\left(\frac{\eta_{T,B}}{\eta_{20,w}}\right)\frac{(1-\bar{v}p)_{20,w}}{(1-\bar{v}p)_{T,B}}$$

Experimentally determined s values are then compared to the theoretical maximum s determined by Eq. 5. Values equal to or lower than the theoretical sedimentation velocity coefficient for a macromolecule of a given size indicate a monomeric oligomerization state. Higher order oligomers are characterized by the degree of positive deviation from the theoretical maximum s value.

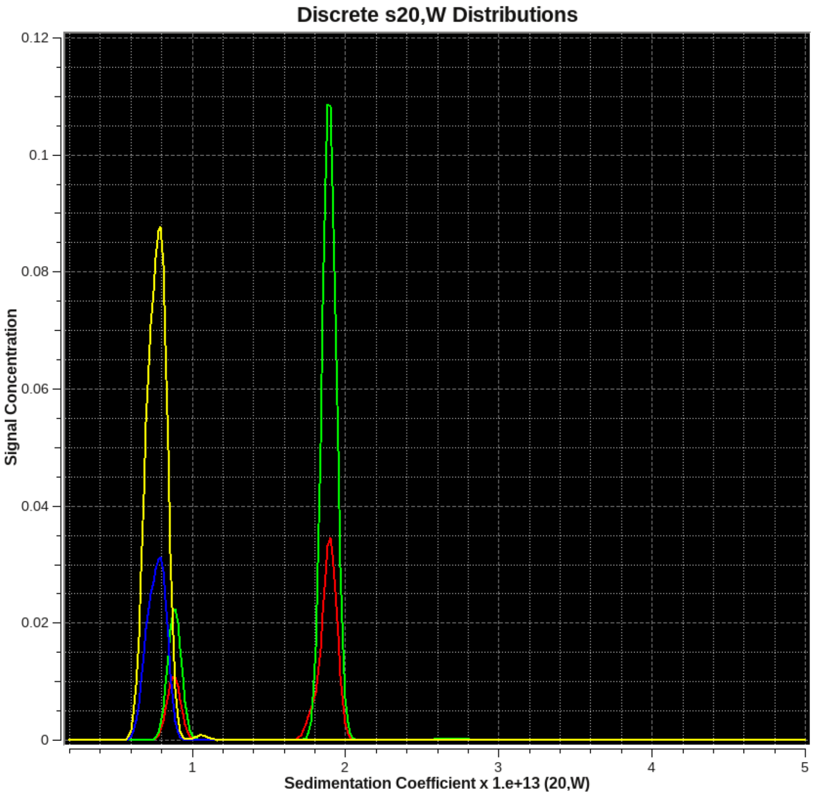

Figure 4.3 Analytical ultracentrifugation corrected sedimentation coefficient velocity plot (blue) 0.3 OD at 280 nm, pH 7.0; (yellow) 0.9 OD at 280 nm, pH 7.0; (red) 0.3 OD at 280 nm, pH 4.45; (green) 0.9 OD at 280 nm, pH 4.45.

The $s_{20,w}$ of ~0.9 is observed solely at the neutral pH structure, is consistent with the expected sedimentation coefficient velocity for monomeric L40 F63W F70W F92F.

Decreasing the pH to 4.4 results in a ~two fold increase in $s_{20,w}$ (Figure 4.3), consistent with formation of a trimer, although roughly 25% of the population appears to be retained in monomeric structure. A three-fold increase in concentration of L40 F63W F70W F92F from 0.3 OD to 0.9 OD at 280 nm effectively yields no change in population distribution from between monomer and trimer, suggesting the monomer present at low pH is structurally compromised and therefore unable to properly assemble into the trimer. In addition to oligomerization state, the experimentally determined frictional coefficient can be used to determine equilibrium constants, e.g. Kd and koff rates. The Kd value for the L40 F62W F70W W92F peptide was determined to be $1.89e^{-7}$ M.[2] Typical Kd values for reversible biological oligomers fall into the micomolar to millimolar range.[33, 34] This low experimentally determined Kd indicates a high affinity for oligomeric state and is consistent with the population distribution greatly favoring formation of the trimer.

4.3.3 pH Dependent Fluorescence Emission Spectra

Fluorescence spectroscopy is ideally suited for detecting changes in solvation of Trp residues elicited from changes in environment due to folding and/or oligomerization. Folding and hierarchal organization to a trimeric structure may lead to burial of the Trp residue within the trimeric core resulting in an increase and blue shift in fluorescence intensity. Analysis of the WT L40 peptide indicates almost no change in the Trp fluorescence emission spectrum between pH 7 and pH 4 (Appendix Figure 4.1), with a fluorescence maximum signal at 358.3 nm for both pH values. Upon a more careful analysis of the low pH crystal structure of the L40 excised from the ectodomain, the penultimate Trp

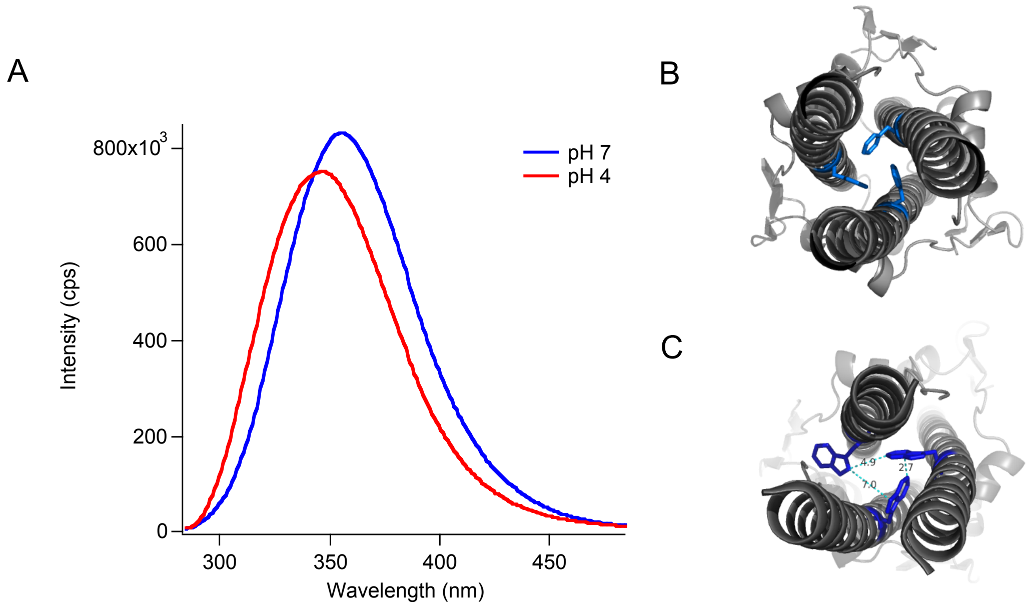

Figure 4.4 (A) pH dependent fluorescence emission spectra and (B) cartoon of Phe packing in WT HA2 and (C) possible packing distribution for Trp when substituted for Phe in acidic HA2 structure (PDB:1HTM)

residue appears to pack on the top of neighboring helices in the trimeric state suggesting that the Trp residue is highly solvated regardless of pH (Appendix A4.1). Ultimately these results suggest that the W92 position is an inadequate position for monitoring pH driven folding by fluorescence spectroscopy. This observation motivated the design of the L40 variants. The L40 mutants were then analyzed for selection of the best candidate that would allow for monitoring L40 folding using fluorescence. The triple mutant L40 F63W F70W F92F, highlighted in this chapter, resulted in a blue-shifted fluorescence emission in response to low pH, however, the relative intensity of Trp decreased with respect to the fluorescence emission of the unfolded structure at neutral pH (Figure 4.4A). This data suggests that the Trp residue is in a more hydrophobic environment in response to a decrease pH but is also involved in a quenching interaction. In the event that the downstream histidine residue may be involved in quenching of the Trp residue, both the L40 F63W F92F and L40 F70W F92F double mutants were examined (data not shown). Examining the distance between Phe from the crystal structures of wildtype HA L40 and possible rotamer conformations of substituted Trp residues (Figure 4.4B), together with the experimental data, ultimately suggest that source of the quenching is a result of an inter-helix Trp-Trp interaction within the trimeric core. This relationship provides an interesting probe to monitor changes within the peptide core.

4.3.4 Equilibrium FTIR

FTIR provides a method for reporting on the finer structural features of the L40 coiled-coil peptide including both solvated (1630 cm^{-1}) and buried helix regions (1645 cm^{-1}) inherent to the coiled coil motif. To more closely examine the L40 F63W F70W F92F structure, temperature dependent absorption spectra were taken in 2 °C increments. Plotting the thermal melt curve at absorbance maximum of 1645 cm^{-1} yields a Tm of 56.9 °C and determined the threshold for aggregation at 72 °C as indicated in the emergence of absorption bands at 1610 cm^{-1} (Figure 4.5). FTIR difference spectra were generated by subtracting the lowest temperature spectrum from each of the high temperatures. Spectra from a well-formed coiled-coil motif should present features of both solvated and buried helix, however, initial analysis showed a single band in the helical region and no clear isosbestic point separating the alpha-helical region and random coil region—a feature indicating a non-two state process (Appendix A4.2). A positive band in the buried helix region at 1645 cm^{-1} indicates formation of buried helix with an *increase* in temperature up to 25°C. Taken together, these results suggest that the trimeric coiled-coil structure is in a cold denatured state between 10-25°C. Regenerating the difference spectra using

25°C as the lower temperature clearly reveals both the solvated and buried helical bands converting to random coil in response to a thermal gradient (Figure 4.5 C-D).

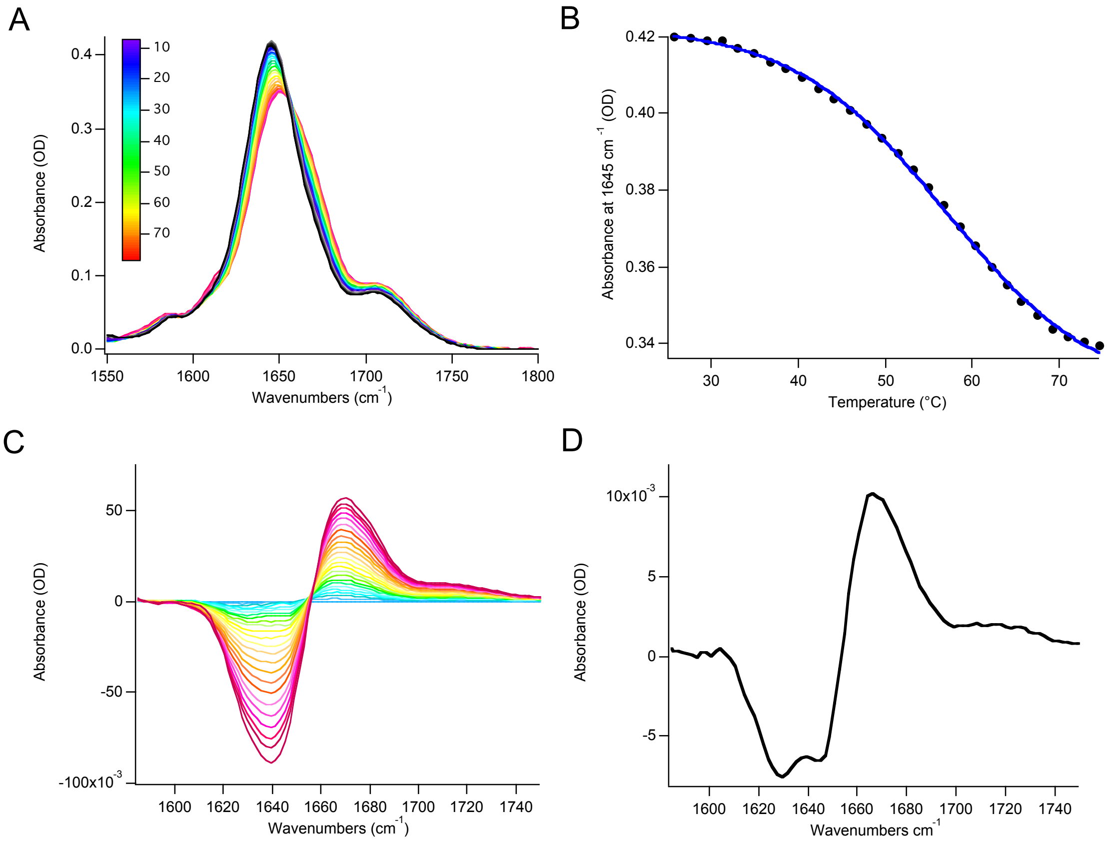

Figure 4.5 Equilibrium FTIR measurements (A) Temperature dependent raw absorbance spectra (B) Thermal melt curve, Tm=57.0°C (C) FTIR difference spectra (D) Expected amplitude change for 10 °C change at a 1.5 mM concentration of peptide. This trace also clearly shows bleach at 1630 and 1645 cm^{-1} representing the solvated and buried helices, respectively and a positive band representing conversion to random coil centered at 1670 cm.$^{-1}$

4.3.5 Kinetic Measurements by Temperature-Jump Infrared/Fluorescence Spectroscopy

Temperature-Jump infrared spectroscopy is an effective way to probe protein folding dynamics, capturing structural changes on the ns-ms timescale. T-jump IR was used in this study to probe the folding dynamics of the L40 F63W F70W F92F peptide. Figure 4.6 shows representative T-jump data collected at a peptide concentration of 2.23 mM. The transient absorption data required a complex four exponential model at both elevated concentration and temperature and were fit to Eq. 6:

$$f(x) = y_0 + A_1 * \exp\frac{\left(-(x - x_0)\right)}{\tau_1} + A_2 * \exp\frac{\left(-(x - x_0)\right)}{\tau_2} + A_3 * \exp\frac{\left(-(x - x_0)\right)}{\tau_3} + A_4 * \exp\frac{\left(-(x - x_0)\right)}{\tau_4}$$

Simpler models were initially tested, however, Arrhenius analysis of the derived rates resulted in negative activation energies for all experimentally observed transient events and therefore these models were rejected (data not shown). For the lower concentration at 1.23 mM, the transient data was fit to two exponentials for the lower temperature and three exponentials for higher temperatures. Table 4.1 summarizes the fit data for 2.23 mM and 1.23 mM taken at 1645 cm^{-1}. The amplitude of the fourth rate is highly concentration dependent and only observed at elevated temperatures and concentration, suggesting that this is a diffusion-limited process and is assigned to recombination of the helices. Arrhenius analysis of this event was not included in Figure 4.6B as analysis of this event results in negative activation energy. This has been previously observed in protein folding reactions and has been attributed to changes in specific heat, $C_{p,}$ of the sample derived from exposure of hydrophobic portions of protein upon unfolding.[35] Although the negative activation energy observed for this process may have some implications for an underlying physical phenomenon, this event is convoluted with the cooling phase of the sample and cannot be confidently analyzed, thus, is not included in the thermodynamic analysis of the L40 peptide. The earliest event at 2-4e^{-6} (s) has little dependence on temperature, suggesting an extremely low kinetic barrier. This phase has been previously reported in folding kinetics of coiled-coil motifs assigned to fraying of helices at the termini of the coiled-coil structure.[22] Analysis of wavelength dependence of the transient events reveals that the second fastest phase ~e^{-5} (s) is observed only in regions probing the buried helix band at 1645 cm,$^{-1}$ as is evident by the lack of this phase in the 1630 cm^{-1} transient data summarized in Appendix A4.3. This event may be related to an off pathway intermediate, e.g. registry shift of the coiled-coil structure, as off-pathway intermediate structures have previously been observed for pH driven coil motifs.[23] The third rate observed ~e^{-4} (s) has the largest apparent temperature dependence, however also displays the greatest amount of noise in the Arrhenius analysis likely from convolution with the slowest rate observed in the transient data. Assignment of this rate will be discussed in the following paragraph describing the L40 peptide analysis by T-jump fluorescence spectroscopy.

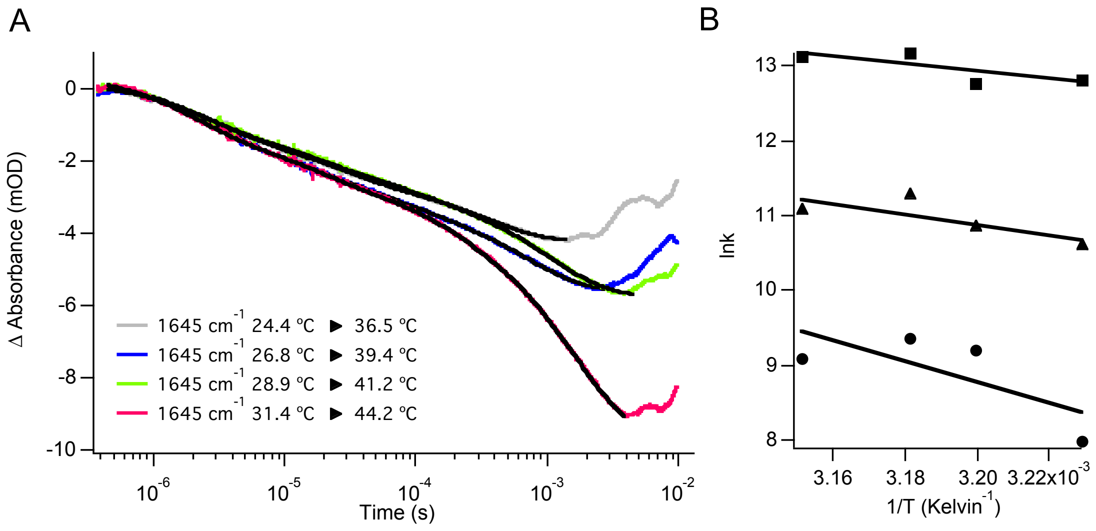

Figure 4.6 Representative T-Jump Infrared transient absorption spectra (A) and (B) linear representation of Arrhenius equation, where the slope of line fit is equal to -Ea/R. The symbols represent individual rates, where squares corresponds to Tau1, triangles to Tau2 and circles represents Tau3. The fourth rate is not included in the Arrhenius analysis as discussed in main text.

[mM]	T-Jump (°C)	Tau1 (s)	A1	Tau2 (s)	A2	Tau3 (s)	A3	Tau4 (s)	A4
2.23	24.4-36.5	2.74 e^{-6}	0.318	2.53 e^{-5}	1.07	3.46 e^{-4}	1.66	NA	NA
	26.8-39.4	2.87 e^{-6}	0.405	1.97 e^{-5}	0.838	1.01 e^{-4}	0.721	7.69e^{-4}	2.34
	28.9-41.2	1.931e^{-6}	0.145	1.28e^{-5}	0.745	8.64e^{-5}	0.889	1.10e^{-3}	2.82
	31.4-44.2	2.02e^{-6}	0.944	1.56e^{-5}	0.9435	1.35e^{-4}	1.04	1.6e^{-3}	5.97
1.23	24.4-40.5	4.39e^{-6}	0.242	7.89e^{-5}	2.85	NA	NA	NA	NA
	26.8-43.0	4.92e^{-6}	0.478	9.47e^{-5}	0.385	5.60e^{-4}	0.407	NA	NA
	28.9-43.2	4.793e^{-6}	0.358	4.74e^{-5}	0.060	4.14e^{-4}	0.222	NA	NA
	31.1-45.1	4.16e^{-6}	0.403	3.83e^{-5}	0.140	3.85e^{-4}	0.328	NA	NA

Table 4.1. Summary of transient infrared absorption data taken at 1645 cm^{-1}

Complementing the T-jump IR data, fluorescence T-jump was preformed probe the folding dynamics from the perspective of the Trp residue buried in the coiled-coil core. Analysis of the resulting transient fluorescence data reveal a single exponential fit associated with a single kinetic event reporting on changes in the environment of the Trp residues (Figure 4.7A). Figure 4.7B is a plot of the corresponding Arrhenius analysis of the single rate observed in the T-jump fluorescence transient data. The fit for the transient data are summarized in Table 4.2. Early starting temperatures give rise to positive transient emission signals indicating loosening of the trimeric core. The loosening of the core subsequently alleviates quenching resulting from inter-helix Trp-Trp interactions, resulting in a positive fluorescence emission signal. Interestingly, initiating the T-jump from higher starting temperatures yields a change in the sign of the fluorescence emission, corresponding to a bleach of the Trp fluorescence emission. At the higher starting temperatures, the trimeric core is presumably already loosened; therefore, the further increase in temperature initiated by the temperature-jump results in exposure of the Trp to bulk solvent yielding quenching of the Trp residue due to solvation. The timescale of this transient event also overlaps with one of the kinetic phases observed in the amide I' transition observed in the T-jump IR experiments. This transient event is therefore assigned to loosening of the trimeric core of the L40 peptide.

Together, the transient infrared and fluorescence data begin to shape a model for the folding of the HA L40 coiled-coil motif (presented in Figure 4.7C). In this model the folding of L40 is achieved through two on-pathway intermediates. I_1 may be assigned to fraying of the termini of the coiled-coil structure. This kinetic phase is conserved among all concentrations and probe frequencies, has the smallest temperature dependence and has previously been observed in dynamic studies of dimeric coiled-coil structures. The second intermediate, I_2, is only associated with the frequency probing the buried helix. This phase may have to do with loss of helical structure or a shift in registry of the

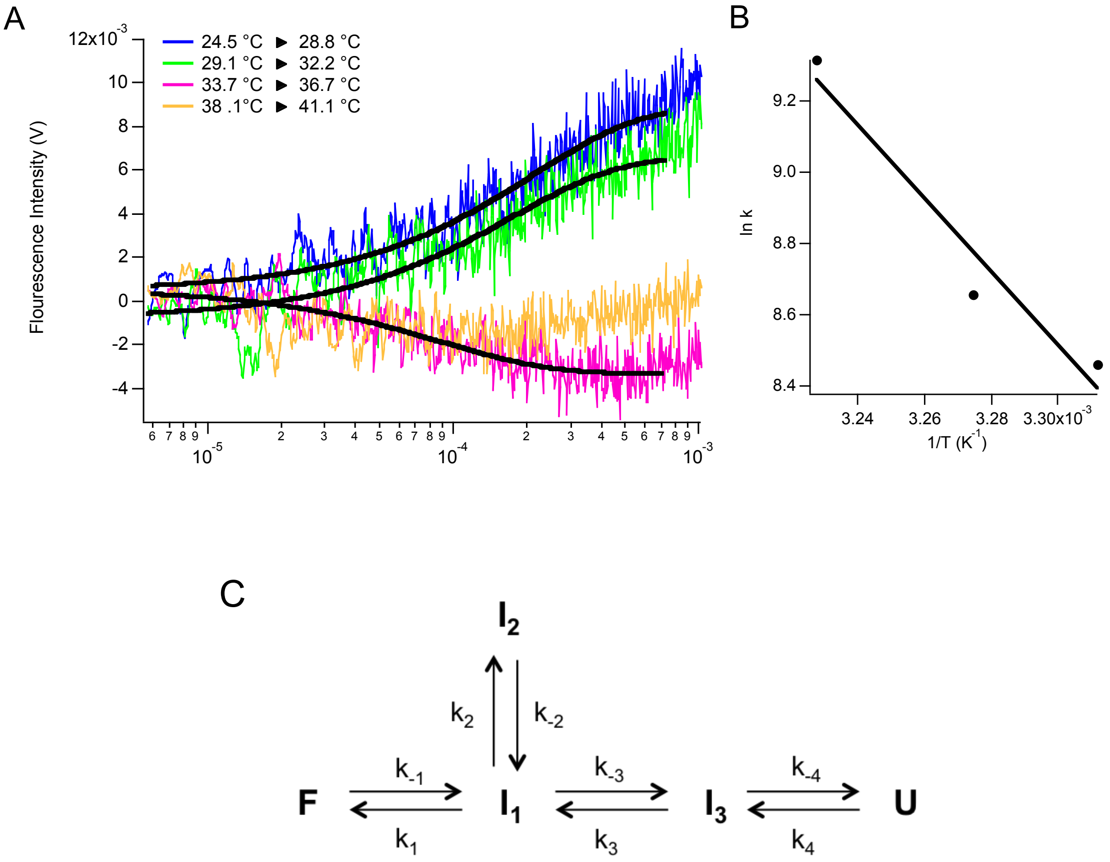

Figure 4.7 (A) Fluorescence t-jump transient data and (B) Arrhenius plot of experimentally determined rates (C) Plausible kinetic scheme of L40 folding

[μM]	T-Jump (°C)	Tau (s)
75	24.5-28.8	2.12 e^{-4}
	29.1-32.2	1.74 e^{-4}
	33.7-36.7	9.02 e^{-5}
	38.1-41.1	NA

Table 4.2 Fluorescence T-jump temperature and fit data reported in Figure 4.7

hydrophobic core; however, further experiments are necessary to adequately assign this intermediate and the associated rate. I$_3$ is relevant to the formation of the hydrophobic core. This intermediate can easily be assigned by the fluorescence t-jump data because in this instance, the Trp residue is sensitive to the local environment of the core structure. Finally, U represents the unfolded structure in which the helices of the trimer are dissociated. The rate associated with this structure is highly concentration dependent and is only detectable at higher concentrations and elevated temperatures.

Setting aside both off pathway and diffusion limited steps, the rates of major events in the folding pathway are quite similar to those observed for folding of dimeric coiled-coil motifs, e.g. the GCN4 leucine zipper, [22] albeit L40 accesses a slightly more complicated folding pathway to achieve the trimeric final structure. GCN4 is also requires multiple steps to achieve folding of the coiled-coil domain and is associated with two primary rates at ~10 μs and ~100 μs,[22] these rates are associated with loosening of the N-termini and formation of the core structure by zipping of the helices, respectively. The models that incorporate these rates ignore diffusion-limited steps such as the initial association of peptides that make the dimer (in the case of GCN4); however, this rate is at least partially accessible in the L40 measurements. The results highlighted in this study correspond nicely with those of GCN4 and it would appear that steps involving loosening of the oligomer termini and formation of the core structure are conserved between folding of a coiled-coil dimer and folding of a coiled-coil trimer.

4.4 Conclusions

In summary, this chapter aimed to study the folding dynamics of an essential component of the influenza hemagglutinin mechanism, hypothesized to be responsible for the early conformational response of HA in the acidified endosome. Folding of the L40 peptide aids in priming the HA fusion peptide for insertion into the host membrane, extending the fusion peptide to the membrane surface. In this study, a portion of the HA2 domain representing the pH sensitive trigger, L40 peptide, was synthesized and modified to incorporate spectroscopic probes sensitive to the core of the peptide structure by mutating Phe in the core to Trp residues. Analysis of the L40 F63W F70W F92F HA2 variant yields folding kinetics where the core structure is formed within a few hundred microseconds. These results are consistent with previous folding studies of coiled-coil motifs such as GCN4, and indicate a non-two-state folding pathway for L40, given that multiple intermediates are detectible in the dynamic measurements. The implications of these studies for folding of the full-length HA protein suggest that the coiled-coil motif is rapidly formed and generates a tightly associated helical bundle. In conclusion, this study aims to reveal finer mechanistic details regarding the folding dynamics of HA2 L40 peptide. Results from this model can be used to refine theoretical models describing HA folding and peptide mediated fusion in vivo.

4.5 References

1. Morens, D. M. and Anthony S. Fauci, A. S. The 1918 Influenza Pandemic: Insights for the 21st Century.J Infect Dis. 2007, 195, 7, 1018-1028. J Infect Dis. (2007) 195 (7): 1018-1028.

2. Shinya, K., Makino, A., Kawaoka, Y. Emerging and Reemerging Influenza Virus Infections. Veterinary Pathology. 2010, 47(1), 53-57.

3. Neumann, G., Noda, T., and Kawaoka, Y. Emergence and pandemic potential of swine-origin H1N1 influenza virus. Nature. 2009, 459, 931-939.

4. Lambert, L. C. and Fauci, A. S.Influenza vaccines for the future. N. Engl. J. Med. 2010, 363, 2036-2044.

5. Krammer, F. and Palese. Advances in the development of influenza virus vaccines. Nature Reviews Drug Discovery. 2015, 14, 167–182.

6. Eckert, D. M. and Kim, P. S. Mechanisms of viral membrane fusion and its inhibition. Annul. Rev. Biochem. 2001, 70, 777-810.

7. Structures of influenza A proteins and insights into antiviral drug targets. Nature Structural & Molecular Biology. 2010, 17, 530–538.

8. Hamilton, B. S. Whittaker, G. R. and Daniel, S. Influenza Virus-Mediated Membrane Fusion: Determinants of Hemagglutinin Fusogenic Activity and Experimental Approaches for Assessing Virus Fusion. Viruses 2012, 4, 1144-1168 .

9. Carr, C. M and Kim, P. S. A spring-loaded mechanism for the conformational change of influenza hemagglutinin. Cell. 1993, 73, 823-832.

10. Itzstein, Mark. The war against influenza: discovery and development of sialidase inhibitors. Nature Reviews Drug Discovery. 2007, 6, 967-974.

11. Harrison, S. C. Viral Membrane Fusion. Nature Structural & Molecular Biology. 2008, 15, 690 – 698.

12. Carr, C.,Chaudhry, C and Kim, P. S. Influenza hemagglutinin is spring-loaded by a metastable native conformation. Proc. Natl. Acad. Sci. 1997, 94, 14306–14313.

13. Onuchic, J. N. et al. Order and disorder control the functional rearrangement of influenza hemagglutinin. PNAS. 2014, 111(33), 12049-12054.

14. Burkhard, P., Stetefeld, J. and Strelkov, S. V. Coiled-coils: a highly versatile protein folding motif.

15. Zhou, N. E., Kay, C. M., Hodges, R. S. Synthetic model proteins: positional effects of interchain hydrophobic interactions on stability of two-stranded alpha-helical coiled-

coils. J. Biol. Chem. 1992, 267, 2664- 2670.

16. Wolf, E. et al. MuiltCoil: a program for predicting two and three-stranded coiled-coils. Protein Sci. 1997, 6, 1179-1189.

17. Chen, Y. A. and Scheller, R. H. SNARE-mediated membrane fusion. Nature Reviews Mol. Cell Biol. 2001, 2, 98-106.

18. Gebauer, F. and Hentze, M. W. Molecular mechanisms of translational control. Nature Reviews: Mol. Cell Biol. 2004, 5, 827-835.

19. Parkinson, J. S., Hazelbauer, G. L. and Falke, J. J. Signaling and sensory adaptation in Escherichia coli chemoreceptors: 2015 update. Trends in Molecular Biology. 2015,23(5), 257–266.

20. Chan, D. C., Fass, D., Berger, J. M. and Kim, P. S. Core Structure of gp41 from the HIV Envelope Glycoprotein. Cell. 1997, 89(2), 263-273.

21. Lee, J. E. and Saphire, E. O. Ebola virus glycoprotein structure and mechanism of entry. Future Virol. 2009, 4(6), 621-635.

22. Wang, T. Lau, W. L.., DeGrado, W. F. and Gai, F. T-jump infrared study of the folding mechanism of coiled-coil GCN4-p1. Biophysical Journal. 2005, 89(6), 4180-4187.

23. Hamm, P. et al. pH-Jump Induced Leucine Zipper Folding beyond the Diffusion Limit. J. Phys. Chem. B, 2015, 119 (4),1425–1432.

24. Durr, E. and Bosshard, H. R. Folding a three stranded coiled-coil. Protein Sci. 2000, 9(7), 1410–1415.

25. Dyer, R. B., Gai, F., Woodruff, W. H., Gilmanshin, R., Callender, R. H. Infrared Studies of Fast Events in Protein Folding. Acc. Chem. Res. 1998, 31, 709-716.

26. Williams, s., Causgrove, T. P., Gilanshin, R., Callender, R. H., Woodruff, W. H., Dyer, R. B. Fast Events in Protein Folding: Helix Melting and Formation in a Small Peptide. Biochemistry. 1996, 35, 691-697.

27. Causgrove, T. P. and Dyer, R. B. Nonequilibrium protein folding dynamics: laser-induced pH-jump studies of the helix–coil transition. Chemical Physics. 2006, 323(1), 2-10.

28. Cooper, T. M. and Woody, R. W. The effect of conformation of the CD of interacting helices: a theoretical study of tropomyosin. Biopolymers, 1990, 30, 657-676.

29. Lau, S.Y., Taneja, A.K., Hodges, R.S., Synthesis of a model protein of defined secondary and quaternary structure. Effect of chain length on the stabilization and formation of two-stranded alpha-helical coiled-coils. J Biol Chem. 1984, 259(21),13253-13261.

30. Lebowitz, J., Lewis, M. S. and Schuck, P. Modern analytical ultracentrifugation in protein science: A tutorial review *Protein Science*. 2002, 11, 2067–2079.

31. van Holde, K.E. and Weischet, W.O. 1978. Boundary analysis of sedimentation velocity experiments with monodisperse and paucidisperse solutes. *Biopolymers* 17, 1387–1403.

32. Teller, D.C., Swanson, E., and DeHaen, C. The translation frictional coefficient of proteins. *Methods Enzymol*. 1979, 61, 103–124.

33. Nooren, I. M. A.; Thornton, J. M. J. Structural characterisation and functional significance of transient protein-protein interactions Mol. Biol. 2003, 325, 991–1018.

34. Ali, M. H., Imperiali. Protein oligomerization: How and Why .Bioorganic and Medicinal Chemistry. 2005, 13, 5013-5020.

35. Obliveberg, M., Tan, T-J and Fersht, A. R. Negative activation enthalpies in the kinetics of protein folding. PNAS. 1995, 92, 8926-8929.

Appendix 4: Characterization of the Folding Dynamics of Hemagglutinin HA2 L40 peptide

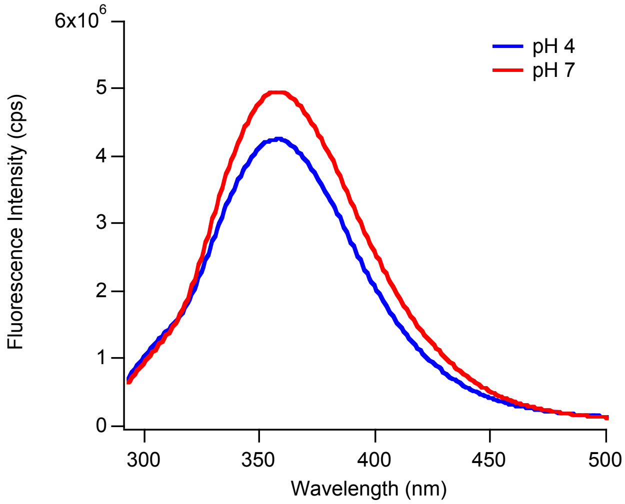

Figure A4.1. Fluorescence emission spectra of WT L40 peptide corresponding to a fluorescence emission maximum of 358.3 nm for both pH 4 and pH 7 samples.

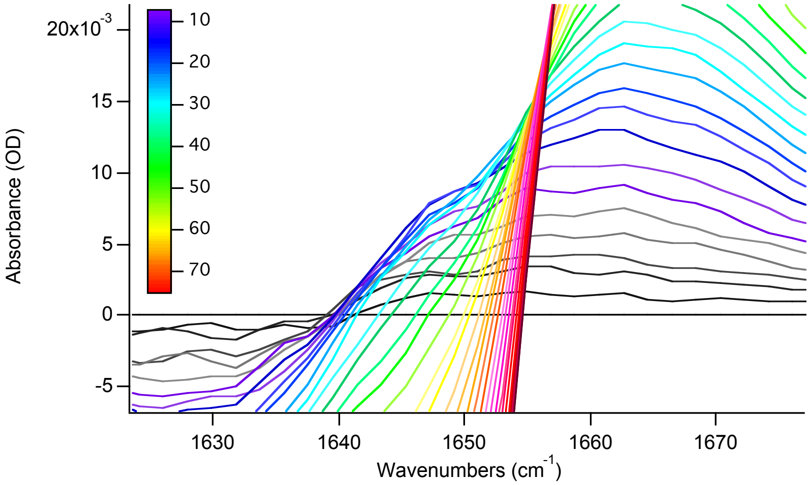

Figure A4.2. Equilibrium FTIR difference spectra generated from using 10 °C as the lower temperature revealing positive absorption band centered at 1645 cm^{-1} indicating cold denatured state from ~10-25 °C

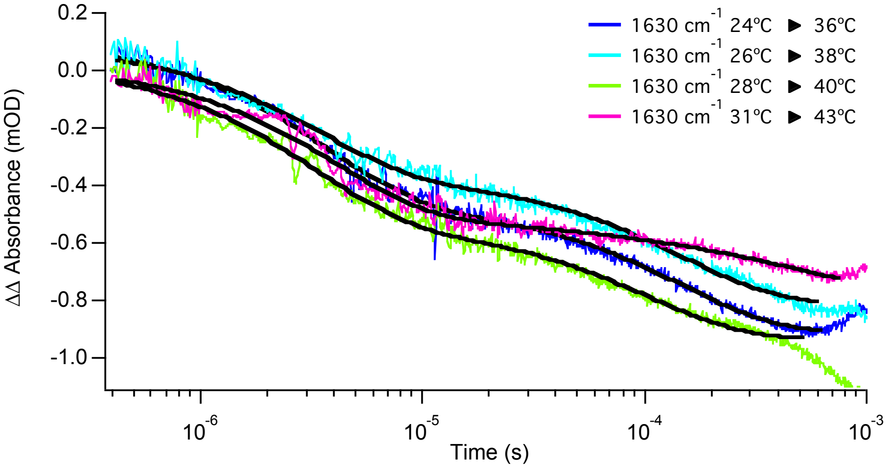

Figure A4.3. Representative T-jump IR transient data for a 1.23mM sample probed at 1630 cm^{-1} demonstrating biphasic kinetics with rates centered at ~4e^{-6} and~3e^{-4} (s)

Chapter 5: Development of an FTIR Assay for Monitoring HA Fusion Peptide Mediated Membrane Fusion

5.1 Introduction:

The general pathway for influenza host cell recognition and infectivity was previously discussed in Chapter 4. This chapter will expand on the concepts put forth in Chapter 4 by briefly focusing on development of a platform for membrane fusion as a consequence of insertion of the hemagglutinin fusion peptide.

5.1.1 Membrane Fusion

Membrane fusion is a process where two contacting membranes merge[1] and is essential to proper cellular function. Examples of the utility of fusion in cellular systems include: mitochondrial function involving mixing of proteins and lipids into the mitochondria; [2,3] reproduction and development,[4,5,6,] where the sperm and egg must merge release of the pronucleus into the oocyte cytoplasm; and vesicular transport and delivery.[7,8,9] The general mechanism of fusion is thought to occur through a hemifusion intermediate[10] where two membranes are drawn within close proximity resulting in contact of outer membrane leaflets of the membrane, ultimately resulting in lipid mixing and formation of a hemifusion intermediate. This step is then followed by mixing of the inner membrane leaflets -- eventually leading to complete fusion of the

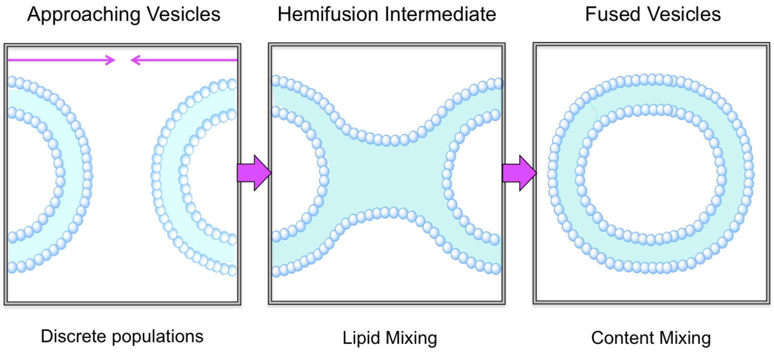

Figure 5.1 A general mechanism for membrane fusion.

membranes.[11] Approaching fusion from a thermodynamic perspective makes it abundantly clear that a significant energy barrier most be overcome in order to achieve fusion. Many biological systems overcome the thermodynamic barrier for fusion by mediating the process with proteins.[12, 13] In general, proteins are thought to aid in fusion by (1) locally destabilizing the target membrane to promote lipid mixing and (2) promoting membrane proximity by refolding of the fusion proteins.[14, 15]

5.1.2 Viral Membrane Fusion

One such entity that achieves protein-mediated membrane fusion is the common virus. It is generally accepted that the mechanism for viral-mediated membrane fusion involves proteins that are held in an inactive state. Upon activation, the protein undergoes a dramatic conformation rearrangement to allow for exposure of the fusion peptide. Insertion of the fusion peptide into the target membrane serves to anchor the protein to the host membrane. Finally, the two membranes are drawn close together by a second large structural change of the protein.[16] In this model, the driving force to promote fusion is derived from the refolding of the fusion protein.

A classic example of a “triggered” system is influenza hemagglutinin, where, after internalization into the host cell, conformational rearrangements of HA are initiated by acidification of the endosome.[17] Interestingly, the HA fusion peptide can still achieve membrane fusion, even in the absence of the remainder of the ectodomain. [18] This property is attributed to the unique structure the helical peptide assumes on the surface of the membrane. Instead of associating with the membrane in a linear fashion as seen with many antimicrobial peptides, the HA fusion peptide is modeled to form a boomerang-like helical hairpin when inserted into target membranes.[19] Thus, the fusion peptide creates a hook allowing it to anchor in one membrane while inserting into another, ultimately drawing the membranes together to promote fusion. Experimental evidence has bolstered this hypothesis, as mutations that inhibit the structural "kink" necessary to allow the fusion peptide to associate with two separate membranes, completely abolishes fusogenic activity. [19]Despite this evidence, there is still much to be learned about the HA fusion peptide and how it achieves membrane fusion. For example, it is not known how many HA molecules are required to exact fusion in vivo. [20]Therefore, developing experimental methods that report on fusion with molecular details of both the membrane and protein components necessary to execute fusion would be an important advancement in studying the mechanism of HA.

5.1.3 *Current Approaches to Studying Membrane Fusion*

There are a number of elaborate membrane fusion assays available, all primarily based on florescence. [21, 22] Typical assays require either dyes at high enough concentrations to promote self-quenching and/or the use of fluorphore modified lipids. A typical assay usually reports on membrane fusion by observing an increase in fluorescence intensity as a result of quenched fluorphores being diluted via fusion with nearby membranes. Although generally helpful, these assay are somewhat laborious and cannot resolve structural details of the fusion components. This chapter describes an FTIR fusion assay using lipid mixtures to detect membrane fusion by the hemagglutinin fusion peptide. This method offers a significant advantage relative to traditional fusion assays in that the structural features of the peptides promoting fusion can be resolved concomitant with changes to the membrane structure. This assay also establishes a method that could easily be translated into studying the dynamic processes driving membrane fusion by methods described earlier in this dissertation.

5.2 Materials and Methods

5.2.1 Peptide Synthesis and Purification

The HA fusion peptide is coupled to a peptide solubility tag (indicated in []): GLFGAIAGFIENGWEGMIDGWYG[GAGKKKK], and was synthesized by standard Fmoc solid phase peptide synthesis utilizing acid-amine coupling on a Liberty 1 peptide synthesizer (CEM, Matthews, NC) using a rink-amide resin. Fmoc protected amino acids were purchased from AnaSpec, Inc. (Fremont, CA). Purification of the FP peptide was completed on a reverse phase C18 column (Phenomenex, Torrance, CA) with TFA as a counterion using a linear gradient of water and acetonitrile. The mass of the purified peptide was confirmed by MALDI-MS using CHCA matrix dissolved in 50:50 mixture of water: acetonitrile. MS confirmed the presence of the fusion peptide with a mass equal to 3202 amu. The peptide was then subjected to two cycles of acid exchange in 20 mM solution of HCl to remove TFA for FTIR experiments.

5.2.2. Circular Dichroism

The secondary structure of the peptide was confirmed by circular dichroism (CD). CD was performed on a JASCO J-810 spectrophotometer equipped with a PFD-425S Jasco temperature controller (Jasco, Inc., Easton, MD). The peptide was dissolved in sodium phosphate buffer, pH 7 at a 30 μM final peptide concentration. The samples were then transferred to a quartz cuvette with a 1 mm path length. The scanning range of the instrument was set between 190-260 nm at a scan rate of 100 nm/min with a 2 s response time and 2 nm bandwidth.

5.2.3 Fluorescence Emission

Fluorescence measurements were taken on a Flouromax spectrophotometer (Horiba Scientific, Edison, New Jersey). The 30 μM peptide samples were dissolved in 20 mM sodium phosphate buffer, pH 7.4, before transfering to a 1 cm fluorescence cuvette. Data was collected using 3 nm excitation and emission slit widths, exciting Trp at 280 nm with an integration time of 1 s over a total range of 285-550 nm.

5. 2.4 Equilibrium FTIR

The temperature dependent equilibrium FTIR experiments were carried out on a Varian 3100 Excalibur FTIR spectrophotometer coupled to a liquid nitrogen cooled mercury cadmium (MCT) detector. Samples were prepared in a split IR cell with a 126 μm Teflon spacer between two CaF_2 windows in a copper housing. Temperature dependent measurements were collected for both the reference (20 mM sodium phosphate buffer, 100 mM NaCl, pH 7) and sample. Each spectrum is composed of an average of 134 scans at 0.5 cm^{-1} resolution.

5.3 Results and Discussion

5.3.1 Confirmation of Secondary Structure by Circular Dichroism.

The hemagglutinin fusion peptide has been shown to adopt an alpha helical conformation in the presence of membranes. To confirm proper folding of the HA fusion peptide CD was performed. The resulting CD spectra yield the expected alpha helical signature in the presence of membranes. As expected, an increase in temperature above the lipid Tm results in an increase in helical content as evident by the 222 nm band in Figure 5.2.

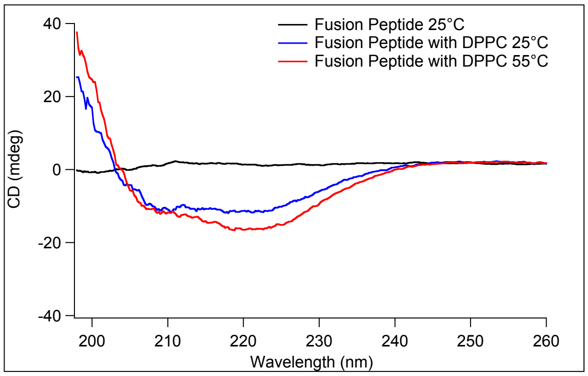

Figure 5.2 CD of fusion peptide comparing structure above and below the Tm of the membrane (Tm_{DPPC}=41°C).

5.3.2 Confirmation of Insertion by Fluorescence Emission Spectra

Similar to the characterization of peptide insertion in Chapter 3, insertion of the fusion peptide into the hydrophobic membrane core should also yield both an increase

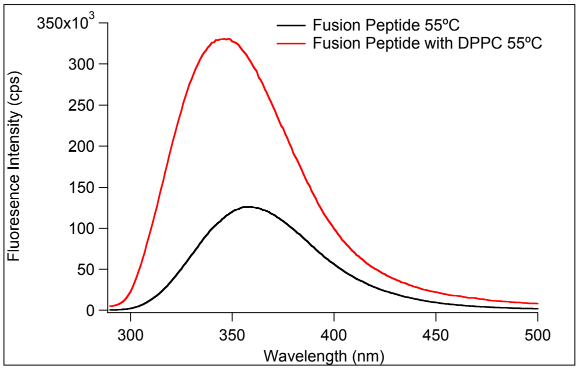

Figure 5.3 Fluorescence emission spectra of HA FP with and without membrane, above the Tm of the DPPC model membranes.

and blue shift of the fluorescence intensity maximum. To test this, the fluorescence of the fusion peptide was measured in the presence and absence of membranes, thus yielding the expected emission pattern for a protein inserting into the membrane (Figure 5.3).

5.3.3 Infrared Fusion Assay

An infrared assay was developed to detect membrane fusion in addition to reporting on other processes that may be critical to fusion, i.e. fusion peptide insertion and/or peptide self-association. The simple experimental scheme to achieve this involves making two separate populations of vesicles, one from per-deuterated DPPC lipids and the other from protonated DPPC lipids. The CD_2 stretch of deuterated lipids has a unique

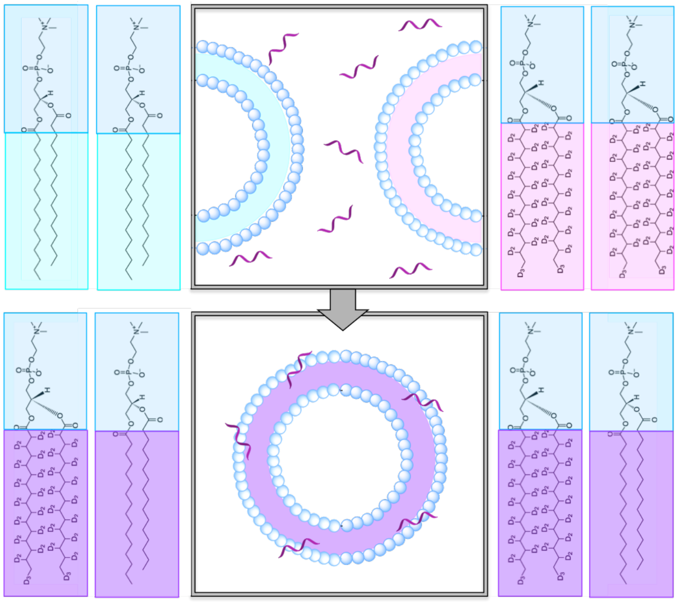

Figure 5.4 Experimental scheme of fusion assay where two homogeneous vesicle populations are added to a solution of fusion peptide. Insertion and subsequent fusion of membranes would result in a spectral shift detectable by IR.

stretching frequency compared to that of the CH_2 lipids, a relationship that can be predicted from the reduced mass equation. It can also be assumed that a mixture of these two populations of lipids would perturb the extensive coupling of the acyl chains observed in homogenous lipid vesicles, a deviation that can easily be detected by infrared spectroscopy. Figure 5.4 shows the experimental scheme for this infrared-based fusion assay.

To first validate the assumed shift in a mixed vesicle population, vesicles were prepared using 50/50 mixture (mole percent) of d62-DPPC and non-deuterated DPPC lipids. The infrared absorbance of this mixture was determined and compared to the infrared absorbance spectra of homogeneous lipid vesicles composed of either d62-DPPC or non-deuterated DPPC lipids. This control was designed to identify the unique infrared signature reporting on the coupling between the deuterated and non-deuterated acyl chains. The results of this positive control are summarized in Figure 5.5.

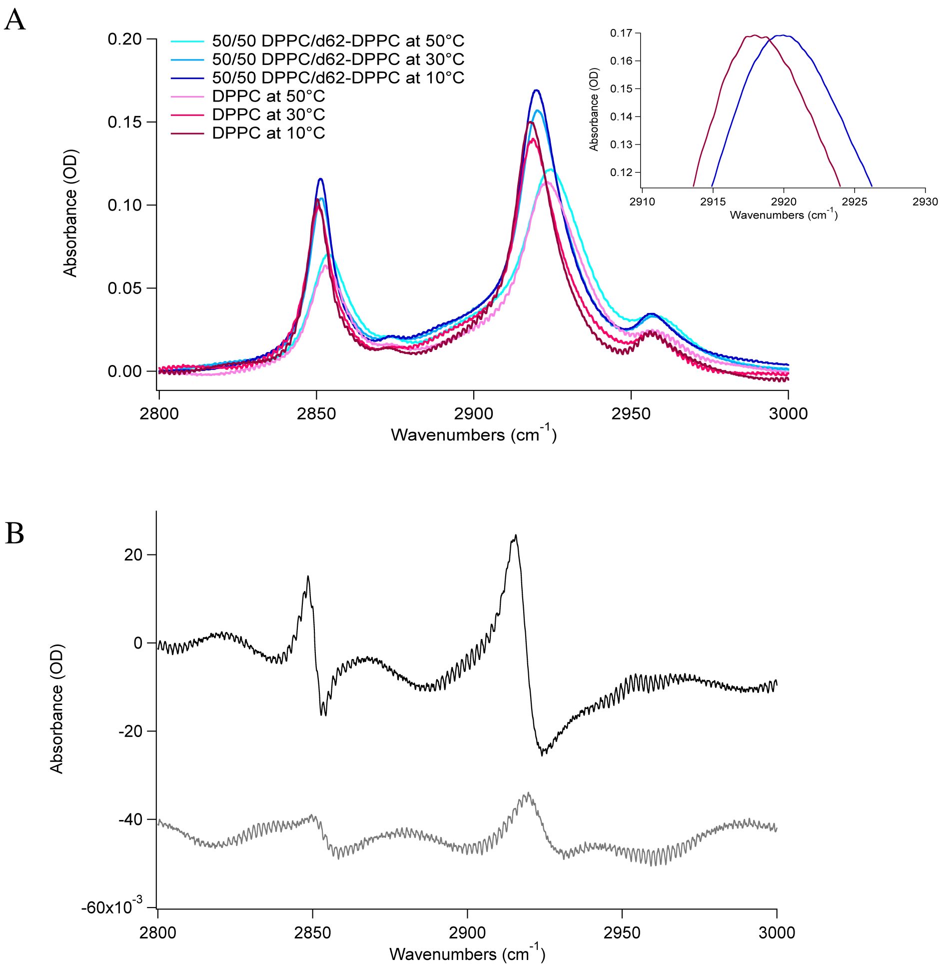

Figure 5.5 (A) Temperature dependent FTIR of pure DPPC vesicles and vesicles composed of 50/50 d62-DPPC/DPPC. The inset image represents normalized IR absorbance data showing (B) The second derivative of absorbance data demonstrating obvious peak broadening of the 50/50 mixture shown in A, where light grey represents the gel phase and black represents the fluid phase.

From the analysis of Figure 5.5, it is clear that pure DPPC has an absorbance maximum at 2917.9 cm,$^{-1}$ whereas the 50/50 DPPC d62-DPPC mixture shifts the absorbance maximum to 2919.9 cm^{-}.^{1} Additionally, Figure 5.5B clearly demonstrates broadening of the 50/50 mixture as is evident by the derivative like features. Importantly, this data indicates the shift induced from mixing lipid populations is a viable probe for monitoring membrane fusion.

Next, the basal level propensity for membrane fusion was tested by comparing the infrared absorbance of pure DPPC vesicles below and above the thermal transition to a sample containing pure DPPC vesicles mixed with pure d62-DPPC vesicles (results summarized in Figure 5.6 and Table 5.1). These data show that there is no significant change in absorbance signal between DPPC vesicles and the sample containing discrete populations of the deuterated and non-deuterated vesicles, suggesting that there is no membrane fusion between the two populations at the timescale of these measurements.

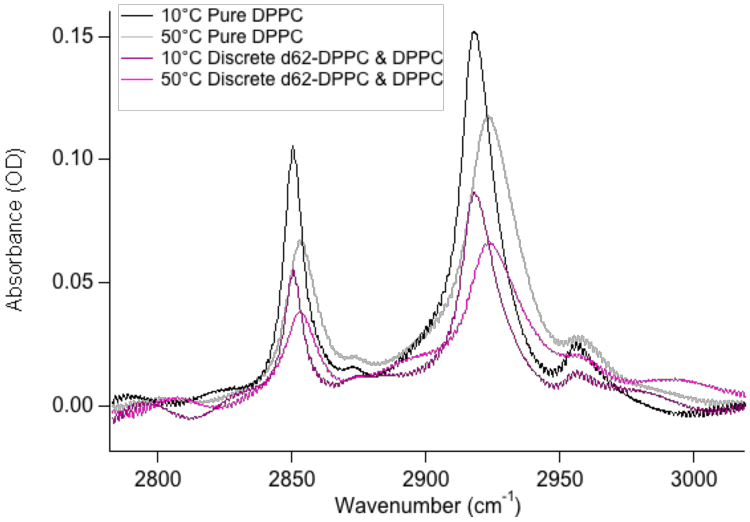

Figure 5.6. FTIR absorbance spectra showing the negative control for membrane fusion.

Temperature (°C)	Pure DPPC (cm^{-1})	Discrete populations of d62-DPPC and non-deuterated DPPC (cm^{-1})
10 °C	2917.9	2917.8
30 °C	2918.8	2918.1
50 °C	2923.0	2923.6

Table 5.1 Summary of frequency shifts for data shown in Figure 5.6.

Finally, to test for the possibly of detecting membrane fusion, discrete populations of homogeneous d62-DPPC vesicles and DPPC vesicles were mixed in the presence of HA fusion peptide. This data is summarized in Figure 5.7 and Table 5.2. These data suggest that the frequencies associated with the infrared regions of the CH$_2$ symmetric and asymmetric lipid stretches are consistent with the FP in assisting in fusion of two discrete vesicle populations. This is evident from the energy of the frequencies achieved in the presence of fusion peptide relative to those observed from deliberate mixing of d62-DPPC lipid with the non-deuterated form.

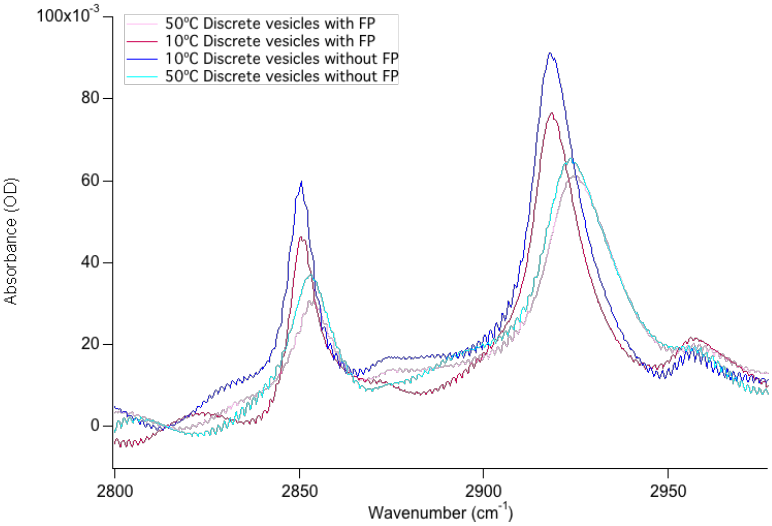

Figure 5.7. FTIR absorption spectra detecting membrane fusion in the presence of fusion peptide

Temperature (°C)	**- Fusion Peptide (cm^{-1})**	**+ Fusion Peptide (cm^{-1})**
10 °C	2917.8	2918.5
30 °C	2918.3	2919.3
50 °C	2923.6	2925.0
50 °C (35 min)	2923.4	2925.3

Table 5.2 Summary of maximum absorbance frequencies from Figure 5.7.

5.4 Conclusions and Future Directions

This chapter highlights preliminary results focused on using infrared as a method to detect membrane fusion. The fusion assay developed in this study was designed such that HA FP mediated fusion could be detected using the frequency shift observed when mixing a pure population of DPPC with d62-DPPC lipids as a result of membrane fusion. Importantly, membrane fusion mediated by the HA fusion peptide was detected by directly probing frequencies associated with the membrane, a feat accomplished without with used of perturbing labels. These promising results suggest that the utility of this platform may be expanded in future studies to examine a number of fusion peptide variants as well as other vital interactions of peptides and membranes necessary to achieve membrane fusion.

5.5 References

1. Martens, S. and Harvey T. McMahon, H. T. Mechanisms of membrane fusion: disparate players and common principles. Nature Reviews: Mol. Cell Biol. 2008, 9, 543 – 556.

2. Chan, D. C. Mitochondrial fusion and fission in mammals. Annu. Rev. Cell Dev. Biol. 2006, 22, 79–99.

3. Praefcke, G. J. & McMahon, H. T. The dynamin superfamily: universal membrane tubulation and fission molecules? Nature Rev. Mol. Cell Biol. 2004, 5, 133–147.

4. Kaji, K. et al. The gamete fusion process is defective in eggs of Cd9-deficient mice. Nature Genet. 2000, 24, 279–282.

5. Le Naour, F., Rubinstein, E., Jasmin, C., Prenant, M. and Boucheix, C. Severely reduced female fertility in CD9- deficient mice. Science 287, 319–321.

6. Miyado, K. et al. Requirement of CD9 on the egg plasma membrane for fertilization. Science. 2000, 287, 321–324.

7. Stenmark H.,Vitale, G., Ullrich, O. and Zerial, M. Rabaptin-5 is a direct effector of the small GTPase Rab5 in endocytic membrane fusion. Cell. 1995, 83 (3), 423–432.

8. McBride, H. M. et al. Oligomeric complexes link Rab5 effectors with NSF and drive membrane fusion via interactions between EEA1 and syntaxin 13. Cell.1999, 98, 377–386.

9. Christoforidis, S., McBride, H. M., Burgoyne, R. D. & Zerial, M. The Rab5 effector EEA1 is a core component of endosome docking. Nature. 1999, 397, 621–625.

10. Chernomordik, L. V. and Kozlov, M. M. Protein–lipid interplay in fusion and fission of biological membranes. Annu. Rev. Biochem. 2003, 72, 175–207.

11. Leonid V. Chernomordik, L. and Kozlov, M. M. Membrane Hemifusion: Crossing a Chasm in Two Leaps. Cell. 2005, 123(3), 375–382.

12. Sandre,O, Moreaux, L., and Brochard-Wyart, F. Dynamics of transient pores in stretched vesicles. Proc. Natl. Acad. Sci. 1999, 96, 10591–10596.

13. Cohen, F.S. and Melikyan, G.B. The energetics of membrane fusion from binding, through hemifusion, pore formation, and pore enlargement. J. Membr. Biol. 2004, 199 1–

14. Bullouh, P. E., Hughson, F.M., Skehel, J. J., and Wiley, D. C.Stucture of influenza haemagglutinin at the pH of Membrane Fusion. Nature 1994, 371, 37-43.

15. Gibbons, D.L., Vaney, M.C., Roussel, A. Vigouroux, B. Reilly, J. Lepault, M. Kielian, F.A. Rey Conformational change and protein-protein interactions of the fusion protein of Semliki Forest virus. Nature. 2004, 320-325.

16. White, J.M., Delos, S.E., Brecher, M., and Schornberg, K. Structures and Mechanisms of Viral Membrane Fusion Proteins:Multiple Variations on a Common Theme. Crit Rev Biochem Mol Biol. 2008, 43(3), 189–219.

17. Doms, R.W., Helenius, A. and White, J. Membrane fusion activity of the influenza virus hemagglutinin: The low pH-induced conformational change. J. Biol. Chem. 1985, 260 (5), 2973-2981.

18. Steinhauer, D.A., Wharton, S.A. Skehel, J.J., and Wiley, D.C.Studies of the membrane fusion activities of fusion peptide mutants of influenza virus hemagglutinin. J Virol. 1995, 69(11), 6643–6651.

19. Lai, A. L., Park, H. White, J. M. and Tamm, L. K. Fusion Peptide of Influenza Hemagglutinin Requires a Fixed Angle Boomerang Structure for Activit. J. Biol. Chem. 2006, 281 (9), 5760-5770.

20. Günther-Ausborn, S., Schoen, P. Ingrid Bartoldus, I., Wilschut, J. and Stegmann, T. Role of Hemagglutinin Surface Density in the Initial Stages of Influenza Virus Fusion: Lack of Evidence for Cooperativity. J Virol. 2000, 74(6), 2714–2720.

21. Domanska, M. K., Kiessling, V. Stein, A., Fasshaur, D. and Tamm, L. K.Single

Vesicle Millisecond Fusion Kinetics Reveals Number of SNARE Complexes Optimal for Fast SNARE-mediated Membrane Fusion. J Biol Chem. 2009, 284(46), 32158-66.

22. Floyd, D. L. Ragains, J. R., Skehel, J. J., Harrison, S. C. and van Oijen, A. M.Single-particle kinetics of influenza virus membrane fusion. PNAS.2008, 105(40), 15382–15387.

Chapter 6: Conclusions and Perspectives

6.1 Summary

This dissertation aims to develop a platform to study dynamic protein-membrane interactions, specifically focused on the underlying mechanisms that drive spontaneous insertion of peptides into membranes. Characterization of spontaneous peptide insertion has previously been examined by diffusion-limited methods that encumber resolution of faster kinetic processes critical to defining the mechanistic details of peptide insertion. Thus, due to the lack of experimental methods available, many of the details regarding this dynamic process have only been resolved computationally.[1] Furthermore, much of the existing methodology lacks the ability to directly couple membrane dynamics to the dynamics of the interacting proteins. Understanding this relationship is critical to understanding the fundamental driving forces that dictate a number of important processes occurring at or within the surface of a membrane.

To address these limitations, peptide insertion and the corresponding membrane dynamics were studied using infrared spectroscopy coupled to temperature-jump methods, and a number of other biophysical techniques. Infrared is a versatile method that can provide great molecular resolution, while temperature-jump techniques offer the time resolution necessary to capture many of these dynamic interactions. These methods were first applied to investigating the mechanism of the gel to fluid phase transition in model d62-DPPC unilamellar vesicles, as discussed in Chapter 2. Given our hypothesis that the rate of peptide insertion is fast relative to the respective diffusion limit, the rapid dynamics of the gel to fluid phase transition make membrane fluidity an ideal property to exploit when investigating peptide insertion into membranes. As outlined in Chapter 3, introducing a model peptide such as MPX to membranes held deep in the gel phase allows the peptide to equilibrate with the membrane surface effectively creating a barrier that can be experimentally regulated to control peptide insertion, thus avoiding limitations consequence of diffusion. Our results suggest that peptide insertion occurs within a few hundred microseconds and is on a competitive timescale with the full thermal relaxation of the membrane. Coupling our understanding of the physical properties of membranes with techniques capable of resolving rapid dynamics with high molecular resolution allows for the possibility of studying a number of important biological processes occurring at or within membranes.

The second half of this thesis focuses on understanding the underlying mechanism behind membrane fusion directed by the Influenza virus, a process facilitated by insertion and folding of influenza's hemagglutinin protein. Specifically, Chapter 4 examines the folding mechanism of the L40 coiled-coil motif—a structure critical to extension of hemagglutinin in response to acidification of the endosome after viral uptake into host cells. Lastly, Chapter 5 details development of an assay based on principles learned from previous chapters to detect both insertion of peptides and fusion of membranes by infrared spectroscopy. Together, these studies add to the mechanistic picture of how influenza achieves fusion through conformational dynamics of hemagglutinin and provides an avenue for future studies probing insertion and fusion with other HA variants.

6.2 Future Outlook

By understanding simple systems like those highlighted in these studies, we can further develop experimental approaches to studying more complex systems centered around protein insertion and folding of membrane associated proteins. For example, this dissertation does not address dynamics governed by complex lipid mixtures or large proteins, but importantly provides a platform to do so. Studying insertion of small model systems like MPX can guide future studies related to other biological processes including membrane protein folding, signaling pathways and viral systems requiring insertion. Additionally, the relevance of folding of the HA L40 peptide extends far beyond the mechanism of influenza pathogenicity as coiled-coil motifs are predicted to be a part of 2-5% of all proteins based on sequence analysis.[2,3] Furthermore, a majority of helical viral proteins that mediate membrane fusion exist as functional trimers; examples of this beyond influenza include proteins that mediate fusion in both HIV and Ebola.[4,5] Thus, understanding these mechanisms transcends to systems involved in many other biological arenas.

6.3 Other contributions

Beyond contributions to the studies discussed in this dissertation I have also made additional contributions to publications outside of the Dyer group. A List of those publications is given below.

- Li, Sha, Sidorov, Anton N., Mehta, A., Das, Dibyendu, Childers, W. Seth, Schuler, Erin, Orlando, Thomas, Lynn, David G., Patterned phosphotyrosine arrays and Histone H1 Binding. JACS, 2014.
- Zheng, Weiwei; Liu, Yang; West, Ana; Schuler, Erin; Yehl, Kevin; Dyer, R.; Kindt, James; Salaita, Khalid. Quantum dots encapsulated within phospholipid membranes: phase-dependent structure, photostability, and site-selective functionalization. JACS, 2014.

6.4 References

1. Im, W. and Brooks, C.L. Interfacial folding and membrane insertion of designed peptides studied by molecular dynamics simulations. PNAS. 2005, 102 (19) 6771–6776.

2. Szappanos, B., Suveges, D, Nyitray, L., Percel, A., Gaspari, Z. Folded-unfoled cross-predictions and protein evolution: the case study of coiled-coils. FEBS Lett. 2010, 584, 1623-1627.

3. Wolf, E. et al. MuiltiCoil: a program for predicting two-and three-stranded coiled-coils. Protein Sci. 1997, 6, 1179-1189.

4. Weissenhorn, W. et al.The central structural feature of the membrane fusion protein subunit from the Ebola virus glycoprotein is a long triple-stranded coiled coil Proc. Natl, Acad. Sci.1998, 95(11): 6032–6036.

5. Pancera, M. et al. Structure and immune recognition of trimeric pre-fusion HIV-1 Env. Nature. 2014, 514(7523), 455-6.